




Extraordinary electrical performance and uncommon transport behavior in the mullite/cordierite composite ceramics

Ahcene Keziz^{1,*}, Meand Heraiz¹, Linda Aissani², Mohammed Rasheed³, and Taha Abdel Mohaymen Taha^{4,*} 

¹ Department of Physics, Physics and Chemistry of Materials Laboratory, University of M'sila, 28000 M'sila, Algeria

² Mater Science Department, ABBES Laghrour- Khenchela., P.O 1252, 40004 Khenchela, Algeria

³ Applied Sciences Department, University of Technology- Iraq, Baghdad, Iraq

⁴ Physics and Engineering Mathematics Department, Faculty of Electronic Engineering, Menoufia University, Menouf 32952, Egypt

Received: 5 August 2025

Accepted: 8 December 2025

© The Author(s), under exclusive licence to Springer Science+Business Media, LLC, part of Springer Nature, 2025

ABSTRACT

One of the key challenges in developing mullite–cordierite electronic substrates is achieving phase homogeneity and controlling porosity to optimize thermal conductivity while maintaining a controlled microstructure. We produced precursor powder for mullite/cordierite composites (Mu/C Com.) for use in multifunctional substrates and electronic components using the sol–gel technique at low temperatures. The precursor powders for the (Mu/C Com.) were made utilizing SiO_2 and Al_2O_3 oxides, respectively, from $\text{Si}(\text{C}_2\text{H}_5\text{O})_4$ and $\text{Al}(\text{NO}_3)_3 \cdot 9\text{H}_2\text{O}$, respectively. Structural phases were identified using XRD and refined using the Rietveld method. Microstructure, grain size, and elemental composition were examined by SEM/EDX. Density and porosity were measured via Archimedes' method. XRD showed pure crystalline mullite for all compositions, while cordierite remained amorphous. Increasing cordierite content reduced grain size by 55%, lowered porosity, and increased bulk density (up to 2.643 g/cm^3 for Mu-C30). The dielectric constant decreased with both frequency and cordierite content. A temperature-activated rise in ϵ' and ϵ'' above 280°C was observed. AC conductivity followed Jonscher's power law, and activation energies decreased from 0.14 to 0.10 eV with increasing cordierite, indicating facilitated ionic transport. The variation in the maximum imaginary component of the modulus and impedance with frequency implies the presence of a non-Debye relaxation phenomenon. These results demonstrate that dense, sol–gel-derived Mu/C composites exhibit low dielectric loss and stable dielectric behavior at high frequency, making them promising candidates for electronic substrates, high-frequency circuit packaging, and ceramic capacitor applications.

Handling Editor: Xuefan Zhou.

Address correspondence to E-mail: ahcen.keziz@univ-msila.dz; taha.hemida@yahoo.com

<https://doi.org/10.1007/s10853-025-12027-6>

Published online: 21 December 2025

Introduction

Aluminosilicate-based ceramics have garnered considerable attention in the past few years [1–3]. Among the various compositions, cordierite ($2\text{MgO} \cdot 2\text{Al}_2\text{O}_3 \cdot 5\text{SiO}_2$) and mullite ($3\text{Al}_2\text{O}_3 \cdot 2\text{SiO}_2$) have been extensively studied in the literature. Known for their excellent mechanical strength, chemical stability, low coefficient of thermal expansion (α), high resistivity, and low dielectric constant, these composites are highly valued [4–6]. These attributes make cordierite–mullite ceramics well suited for numerous applications, including use as refractory materials and electronic substrates. Given their potential in the electronics industry, numerous studies have investigated their dielectric behavior [7, 8], employing various shaping techniques, for example, slip casting, tape casting, or pressing [9–12].

Dielectric ceramics are widely used as insulating materials in high-temperature environments, prompting extensive research into their dielectric properties [13–15]. A comprehensive study of their dielectric behavior requires analyzing the temperature- and frequency dependence of parameters such as dielectric constant, dielectric losses, and impedance. Factors such as phase composition, synthesis techniques, and thermal processing greatly influence these observations, impacting both the structure and microstructure. Key variables, including porosity, grain size, and defects, play critical roles in defining these properties [16]. Ceramic materials with high dielectric constants and low losses at high frequencies, which are electrically and thermally stable, are suitable for applications in ceramic capacitors, high-speed electronic device coatings, and spark plugs [13]. Several factors can influence the electrical conductivity and conduction mechanism of mullite and cordierite, including composition, synthesis method, and presence of impurities, thermal treatment, number of crystalline phases formed, and porosity [14].

It is essential to note that, although numerous literature reports exist on the dielectric properties of ceramics, high-temperature data on the dielectric constant and loss factor are currently available only for commercial products based on Si_3N_4 and glass ceramics [14]. Furthermore, only a limited number of studies have examined the low-cost fabrication of cordierite–mullite ceramics and their relationship with dielectric properties. None of these studies has assessed how dielectric properties change with increasing temperature [7–9]. In this context and with

the objective of continuing the studies involving the use of substrate materials by using cordierite–mullite technical ceramic. The main objective is to produce a mullite–cordierite composite utilizing the sol–gel technique. This technique includes mixing tetraethyl orthosilicate (TEOS), magnesium nitrate hexahydrate ($\text{Mg}(\text{NO}_3)_2 \cdot 6\text{H}_2\text{O}$), and aluminum nitrate nonahydrate ($\text{Al}(\text{NO}_3)_3 \cdot 9\text{H}_2\text{O}$) based on the stoichiometric formula for mullite–cordierite composition. The formation of composite phases will be monitored using X-ray diffraction across varying temperatures. The structural, microstructural, and dielectric characteristics of mullite ceramics produced through the sol–gel method followed by reaction sintering have been illustrated. Research aims to address current knowledge gaps by thoroughly examining the electrical and dielectric characteristics of (Mu/C Com.). Conductivity values will be comparatively analyzed to evaluate their potential for practical applications in electronic devices and energy storage systems. The goal is to fabricate (Mu/C Com.) with dielectric constants and minimal losses at high frequencies, ensuring their applicability in engineering contexts like high-frequency circuit packaging, electronic substrates, and ceramic capacitors. The electrical and dielectric characteristics of mullite-based materials are known to be significantly impacted by their chemical composition, phase composition, and porosity.

Experimental

Starting materials

In this study, tetraethyl orthosilicate (TEOS) ($\text{Si}(\text{C}_2\text{H}_5\text{O})_4$), 99% purity, sourced from Fluka, along with magnesium nitrate hexahydrate $\text{Mg}(\text{NO}_3)_2 \cdot 6\text{H}_2\text{O}$, and aluminum nitrate nonahydrate $\text{Al}(\text{NO}_3)_3 \cdot 9\text{H}_2\text{O}$, obtained from Biochem Chemopharma, Georgia, USA, were utilized as materials.

Sample preparation

Tetraethyl orthosilicate (TEOS), serving as a source of SiO_2 , was dissolved in ethanol, while aluminum nitrate nonahydrate (ANN) provided Al_2O_3 dissolved in distilled water. Magnesium nitrate hexahydrate (MNH), dissolved in water, supplied MgO for cordierite formation. These chemicals were blended to synthesize a composite material comprising mullite and

cordierite. Six samples—designated Mu-C00, Mu-C10, Mu-C20, and Mu-C30—contained (0, 10, 20, and 30 wt.%) cordierite, respectively (as detailed in Table 1).

TEOS, MNH, and ANN were dissolved separately in ethanol and deionized water. The TEOS-to-ethanol ratio was 1:4 by volume, while the TEOS-to-water ratio was 20:1 by mole. Each component was vigorously mixed with its respective solvent for 30 min to ensure uniformity, followed by combining and stirring briskly at room temperature for 2 h. The solution underwent gelation by incubating at 60 °C for 48 h.

Table 1 Weight percentage (wt.%) composition of the fabricated samples

Samples	Mu wt.%	C wt.%	Al ₂ O ₃ wt.%	SiO ₂ wt.%	MgO wt.%
Mu-C00	100	00	71.8	28.2	0
Mu-C10	90	10	68.1	30.52	1.38
Mu-C20	80	20	64.41	32.83	2.76
Mu-C30	70	30	60.72	35.15	4.13

The resulting gel was then dried for 24 h at 120 °C. The white powder obtained was gathered and processed by grinding with a mortar and pestle.

Compact samples were formed by uniaxially cold-pressing the powder, followed by calcination and sintering at various temperatures (see Fig. 1) to complete the process. This methodical approach aimed to control the composition and microstructure of the (M/C Com.), optimizing their properties for applications such as high-frequency circuit packaging, electronic substrates, and ceramic capacitors.

The SiO₂–Al₂O₃–MgO ternary diagram served as a basis for an initial assessment of the potential phases present in the studied formulations. Figure 2 illustrates that the cordierite–mullite composites Mu-C00, Mu-C10, Mu-C20, and Mu-C30 are located within the mullite, cordierite, and spinel phase region.

Characterization techniques

The phase analysis of mullite samples was conducted utilizing a X-ray powder diffractometer (XRD,

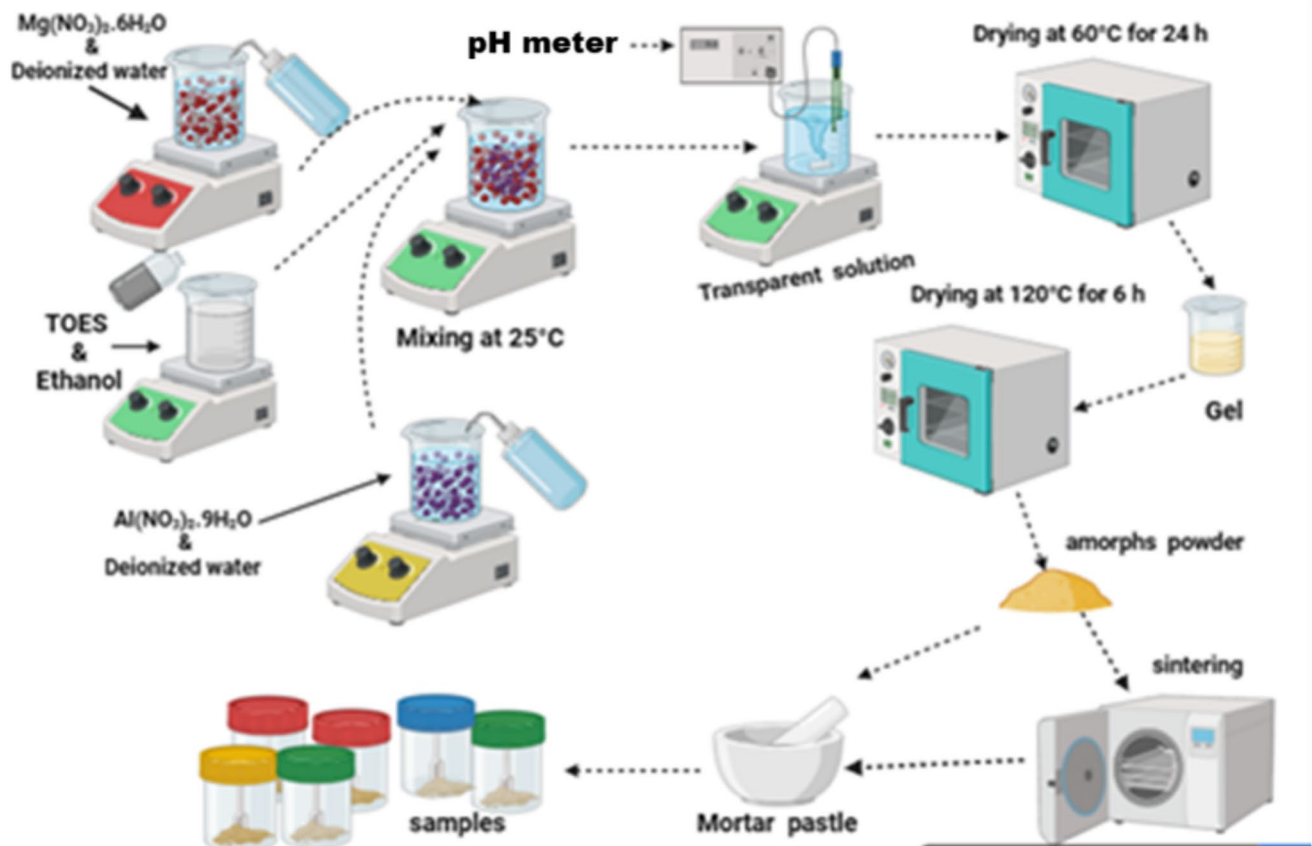
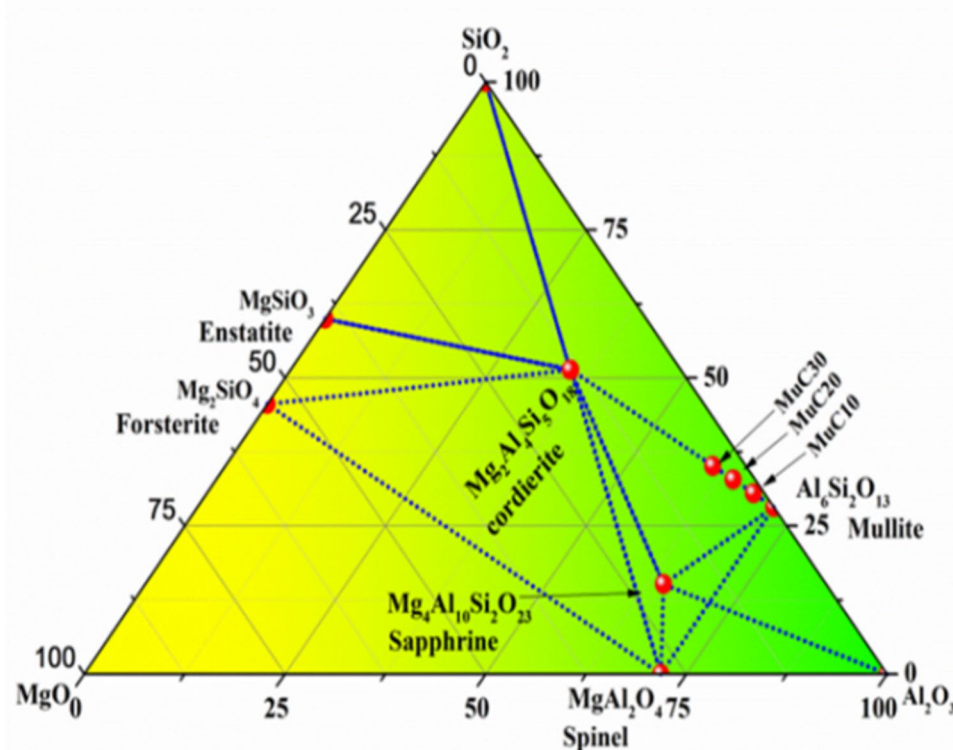


Figure 1 Process flowchart for synthesizing mullite/cordierite composite.

Figure 2 Locations of Mu-C00, Mu-C10, Mu-C20, and Mu-C30 formulations on ternary equilibrium diagram.



model H12, Ultima IV, Japan) with Cu K α radiation ($\lambda = 1.5418 \text{ \AA}$), scanning from 10° to 80° 2θ at 40 kV and 40 mA, with a scan speed of $1^\circ/\text{sec}$. Microstructural properties were employed utilizing a ZEISS scanning electron microscope (SEM) at 20 kV, and AP and BD of sintered samples at 1600°C for 1 h were determined utilizing Archimedes principle. For dielectric measurements, pellets were silver-pasted to create electrodes on opposite sample surfaces and placed in a furnace utilizing a sample holder. AC parameters, including capacitance (C), dissipation factor ($\tan\delta$), and impedance (Z), were measured utilizing an LCR meter (NF model ZM2376, Japan) throughout the frequency bands 100 Hz to 1 MHz. The dielectric constant and AC conductivity were computed, and their changes with frequency (from 100 Hz to 1 MHz) and temperature (from room temperature to 400°C) were investigated.

Results and discussion

Structural characterization

XRD spectra

Figures 3 and 4a, b, c, and d depict the XRD profiles of Mu-C00, Mu-C10, Mu-C20, and Mu-C30 ceramics sintered at 1600°C for 1 h. The spectrum indicates that all samples consist solely of crystalline mullite, with cordierite appearing amorphous. The strength or intensity of mullite increased as the proportion of cordierite in the mullite/cordierite composite samples rose.

Figure 4e, f, and g shows the Rietveld XRD diffraction structure development of the mullite/cordierite composite samples that were heated at 1600°C . The straight lines show calculated levels, while the cross shows real-world data. Below the profile is a graph that shows the difference between the actual and predicted levels. Every design has its Bragg position shown above it. The results show that the actual and estimated standards are very similar, which means that the right structures and starting factors were chosen for the tuning process. The Rietveld XRD analysis of mullite $\text{Al}_6\text{Si}_2\text{O}_{13}$ shows that it has an

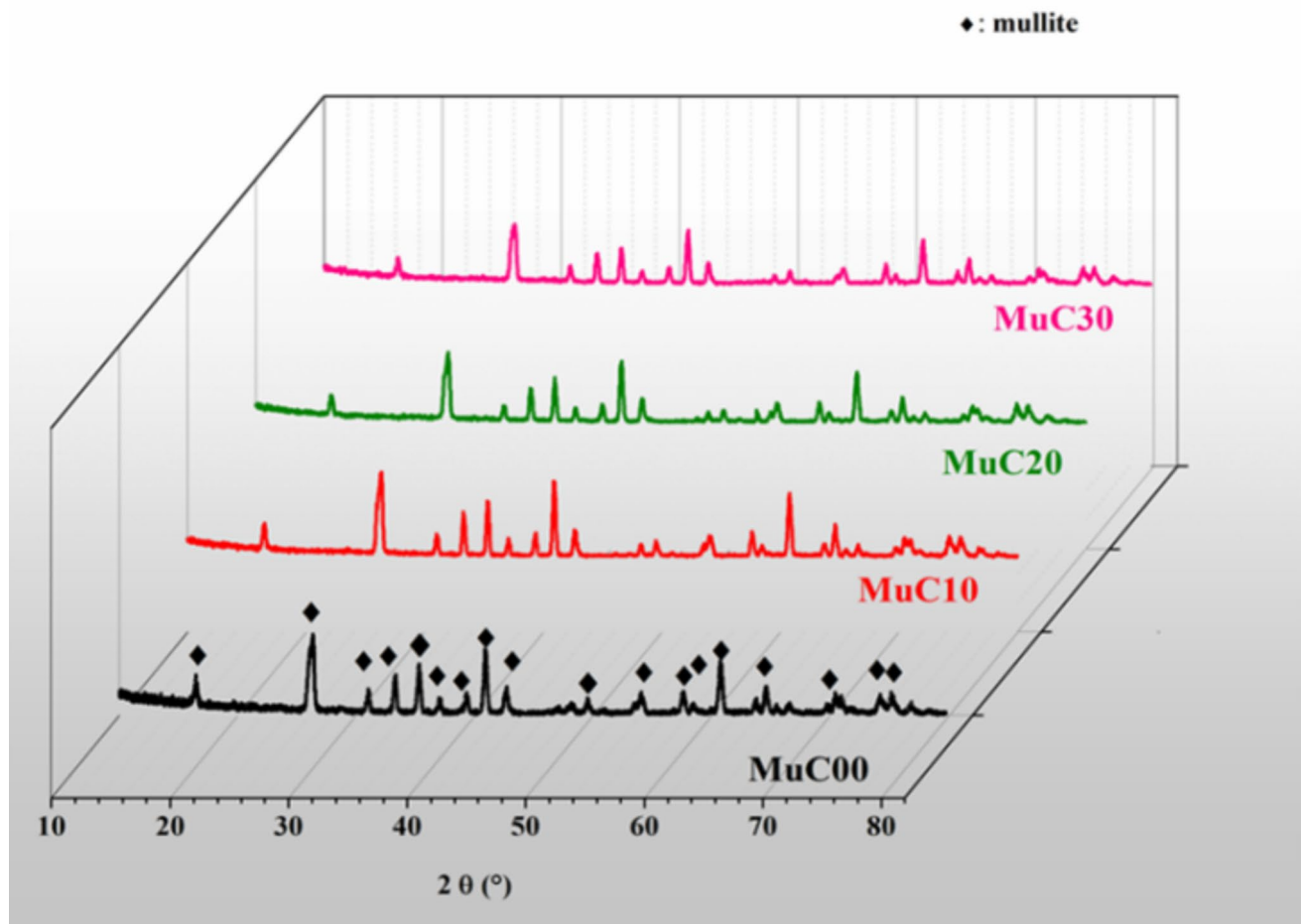


Figure 3 X-ray diffraction profiles of (Mu-C Com.) sintered at 1600 °C for 1 h.

orthorhombic structure and is in the Pbam space group.

The suggested model closely fit the X-ray diffraction pattern of the mullite/cordierite mixtures, but it had low confidence factors. The final Rietveld refinement plot of the mullite/cordierite mixtures is shown in Fig. 4e, f, and g. The image of the unit cell from the Crystals Information File (CIF) is shown in Fig. 4e, f, and g.

The exact data from the structure study of mullite are given in Table 2. We studied the structure of the mullite/cordierite composite sample both as it was made and after being heated to 1600 °C using Rietveld refinement of the X-ray diffraction pattern. This was done to make sure the suggested adsorption process works and to find out exactly where action transfers happen. Profex tools and Vesta were utilized together to look at the scans and investigate the structure.

Microstructural analysis

Figure 5 shows micrographs taken with a scanning electron microscope that show the surface features and microstructure of the sample that was heated to 1600 °C for 1 h. This microstructure showcases a dense assembly of mullite granules with diverse shapes and sizes, and many of them exhibit a porous morphology. Additionally, there are a few grains that exhibit a needlelike form. The surface morphologies and microstructures of the samples sintered at 1600 °C for 1 h were observed under a SEM and are compiled in Fig. 5. Figure 5a evidently shows that sample Mu-C00 lacks cordierite. The microstructure reveals densely packed mullite granules of heterogeneous shapes and sizes, with numerous pores. Some grains appear needle-shaped. In Fig. 5b, for sample Mu-C30, needle-shaped mullite grains are prominently observed, indicating the presence of a glassy phase along grain

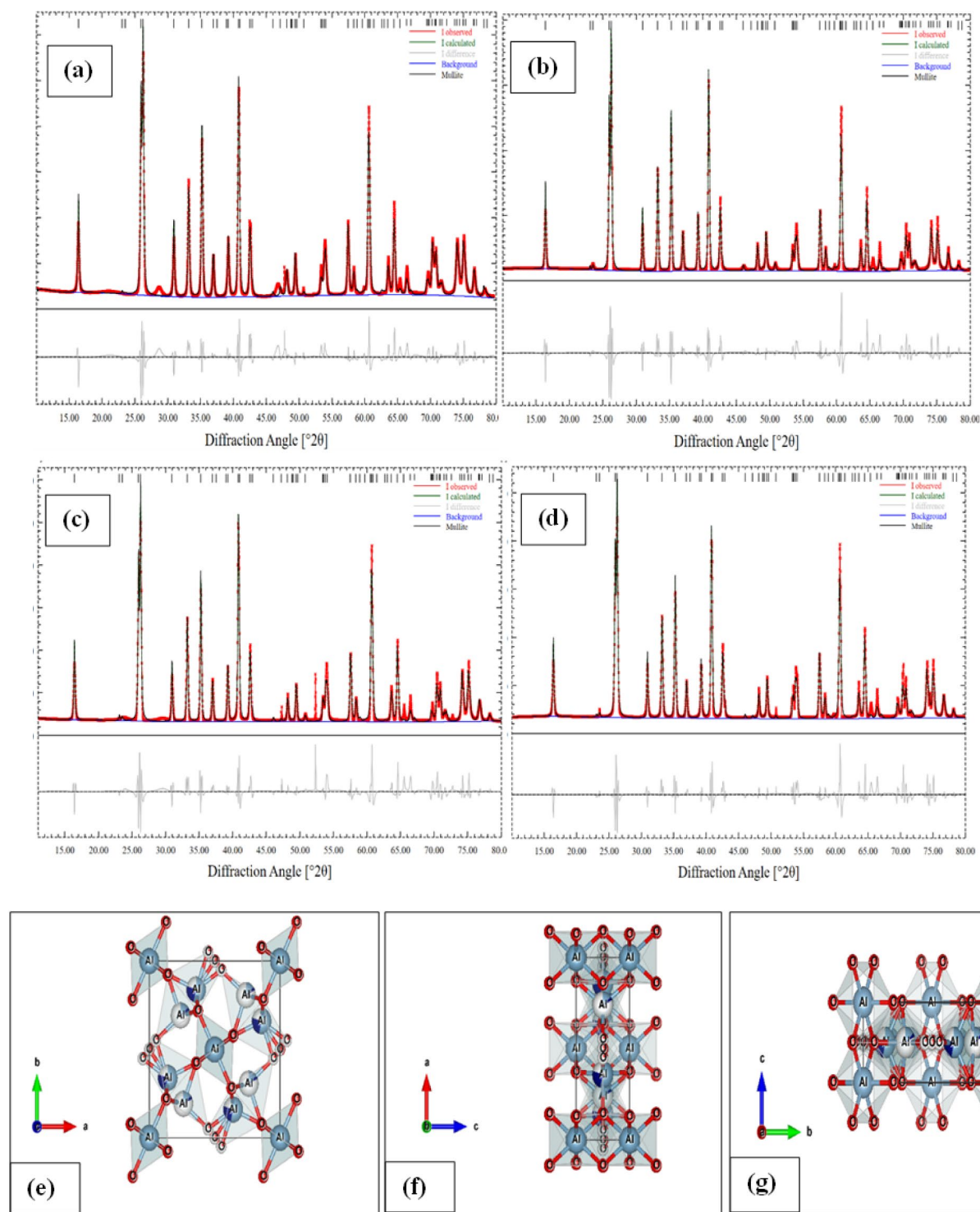


Figure 4 a, b, c, and d Structural characteristics of the mullite/cordierite composites heat-treated samples at 1600 °C as determined from Rietveld refinement of XRD data, and e, f, g unit cell's projection of the (Mu-C Com.).

boundaries due to liquid phase sintering. This facilitates higher density in cordierite-rich materials [14, 17, 18].

Figure 5c–d depicts the grain count versus particle size (μm) for Mu-C00 and Mu-C30 samples, with the distribution following a Lorentzian fitting curve, as

Table 2 Rietveld refinement results of the (Mu-C Com.) heat-treated sample at 1600 °C, focusing on the structural parameters

Phase formula		Mullite “3Al ₂ O ₃ ·2SiO ₂ ”			
Lattice parameters		Space group: Pbam; $\alpha = \beta = \gamma = 90^\circ$			
		Mu-C00	Mu-C10	Mu-C20	Mu-C30
$a(\text{\AA})$		7.55831	7.55320	7.55085	7.55918
$b(\text{\AA})$		7.70574	7.69512	7.6934	7.69964
$c(\text{\AA})$		2.88952	2.88697	2.88637	2.88882
$V(\text{\AA}^3)$		168.29249	167.79872	167.67416	168.13788
Reliability factors	Rwp (%)	12.88	15.90	13.71	12.31
	Rexp (%)	13.13	12.82	13.12	13.53
	χ^2	0.96	1.54	1.09	0.83
	GoF	0.98	1.24	1.04	0.91

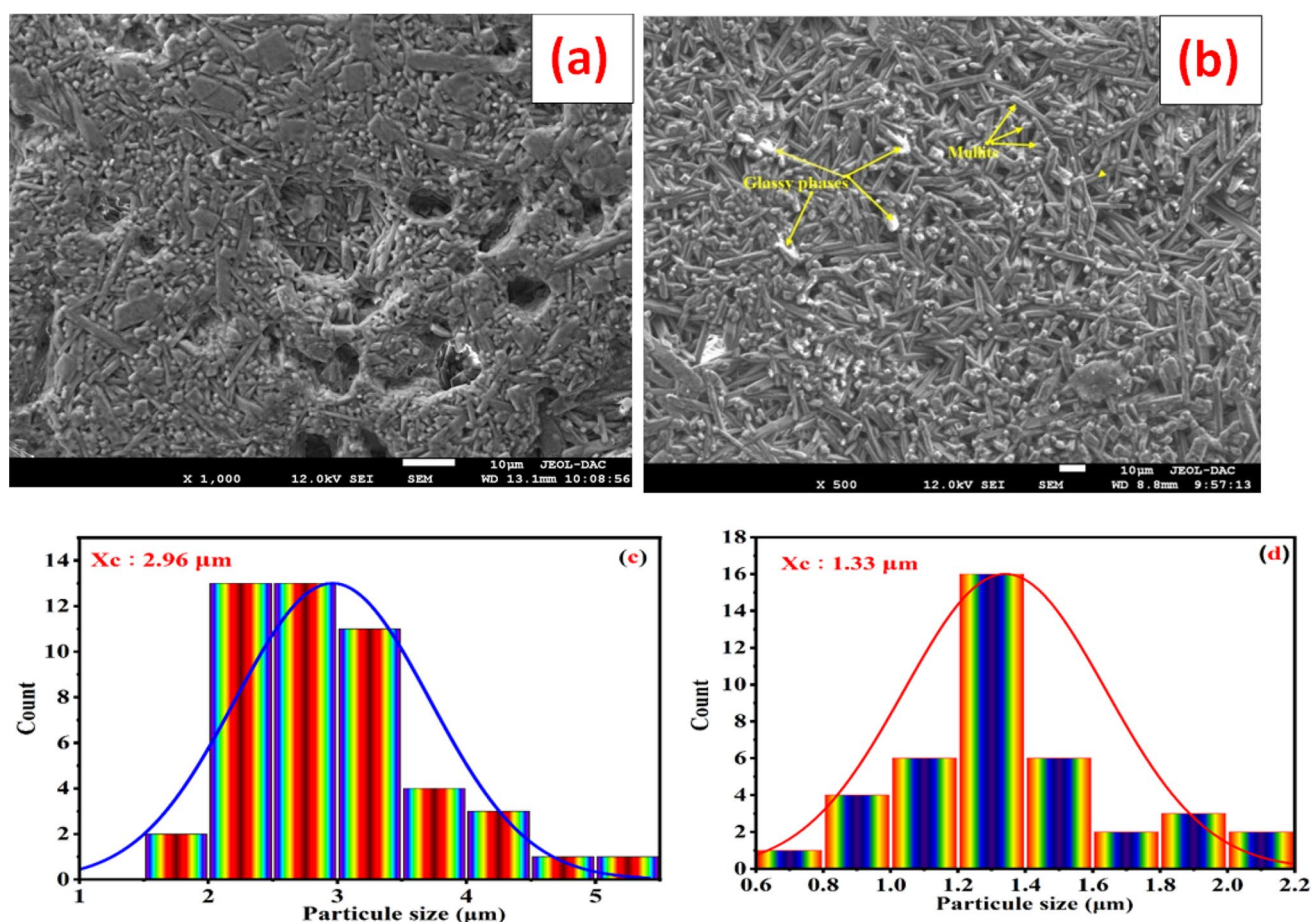


Figure 5 SEM micrographs of (Mu/C C) sintered at 1600 °C for 1 h: **a** Mu-C00; **b** Mu-C30. **c–d** Distribution histogram of grains.

determined by ImageJ analysis of SEM images. The average grain sizes were 2.96 μm for Mu-C00 and 1.33 μm for Mu-C30, indicating a $\approx 55\%$ reduction in grain size.

The chemical composition of the mullite (Mu-C00) and Mu-C30 sintered at 1600 °C for 1 h was assessed utilizing energy-dispersive spectroscopy (EDX), as depicted in Fig. 6.

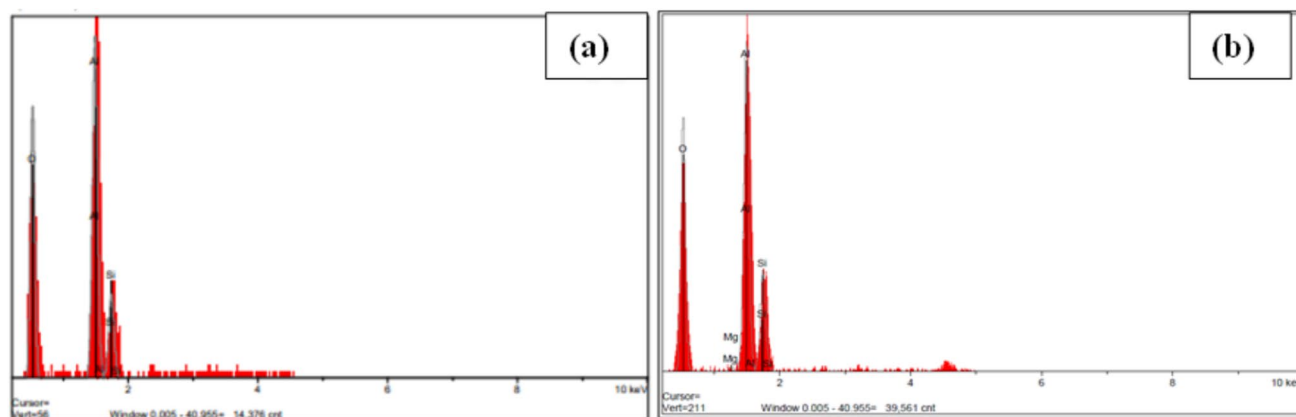


Figure 6 Composition of chemical elements in Mu-C00 and Mu-C30 through mass and atomic percentages.

Table 3 Mass and atomic percentages of chemical elements for Mu-C00 and Mu-C30

Samples	Elements	Conc.%	Atomic%
Mu-C00	O	49.057	62.116
	Al	38.445	29.857
	Si	12.497	9.015
Mu-C30	O	60.40	47.27
	Al	25.40	34.45
	Si	10.85	14.89
	Mg	4.45	4.61

The presence of intended elements (Al, Si, and O) and the absence of impurities in the fabricated samples were verified through EDX analysis, as depicted in Fig. 6a. The weight percentage ratio of aluminum to silicon, determined via EDX analysis and presented in Table 3, closely matches the expected ratio established during the synthesis of the ceramics. Figure 6b shows the EDX analysis, which confirmed the presence of desired constituents (Al, Si, O, Mg) and the absence of any impurity atoms in the prepared samples. The aluminum-to-silicon weight percentage ratios obtained from EDX analysis, detailed in Table 2, correlate well with the ratios specified during the ceramics' synthesis.

Bulk density and apparent porosity (BD and (AP)

To assess the AP and BD of samples at 1600 °C for 1 h, calculations were based on the Archimedes principle [14, 15]. Figure 7 illustrates the relationship between AP and BD of the MCxx composites varying

with cordierite content. As depicted in Fig. 7a, as the amount of cordierite increases, the BD of all samples also increases (Table 4), with the highest BD observed in Mu-C30 sintered at 1600 °C, reaching 2.643 g/cm³. This trend indicates that sample density rises with increasing cordierite content. The enhanced densification at higher temperatures is attributed to increased liquid content in the samples, facilitating densification [19–23]. This aligns with earlier findings from shrinkage analyses, where cordierite transforms into a glassy phase at elevated temperatures, promoting grain rearrangement and higher density [20–24].

Figure 7b illustrates the influence of cordierite on the AP of sintered mixtures at 1600 °C. It shows that AP decreases with increasing cordierite content, suggesting that cordierite dissolves within mullite, generating a glassy phase that aids in the densification process of the samples [4, 25, 26]. The XRD patterns of the sintered samples for 1 h at 1600 °C (Fig. 3) confirm that only the multiple phase is present.

Dielectric analysis

Expression of the relative dielectric constant as a complicated entity including both a real and an imaginary component helps one to grasp the dielectric characteristics of a solid material: $\epsilon^* = \epsilon' - j\epsilon''$, where ϵ' and ϵ'' denote the real and imaginary components of the dielectric constant, respectively. These elements reflect the stored energy in the material as polarization and the energy dissipation under an electric field. Utilizing the following approach, one may recover the actual dielectric constant (ϵ') from complicated impedance data [24, 27, 28];

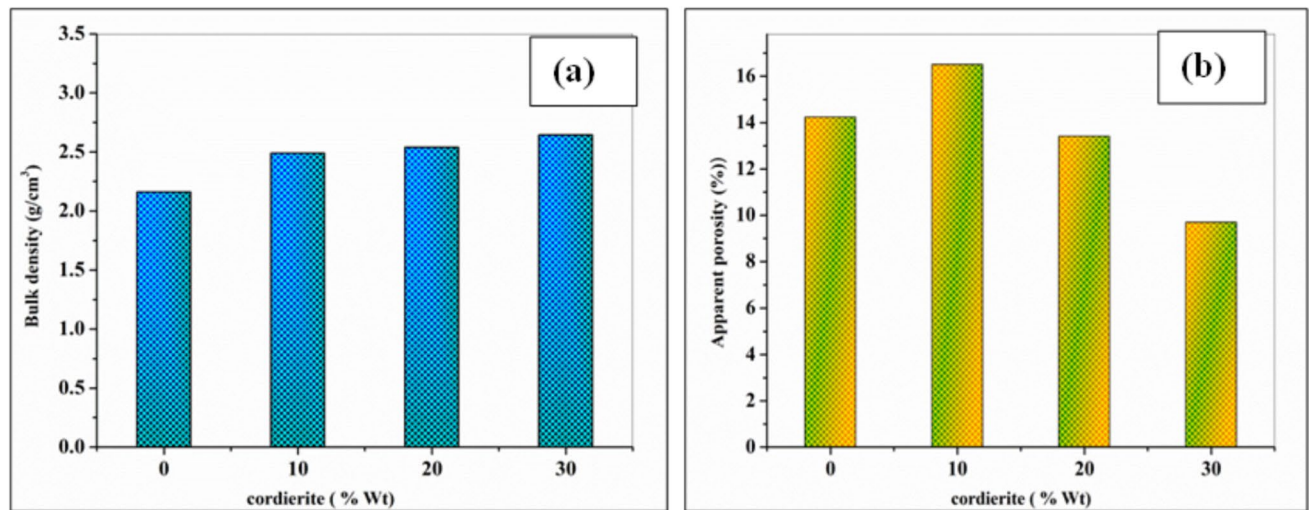


Figure 7 a BD and b the AP of (Mu/C C) sintered at 1600 °C for 1 h, varying with cordierite content.

Table 4 Apparent density and porosity values of the samples at 1600 °C for 1 h

1600 °C		Sample
V_{ap} (%)	BD(g.cm ⁻³)	
14.23	2.159	Mu-C00
16.51	2.489	Mu-C10
13.41	2.537	Mu-C20
9.69	2.643	Mu-C30

$$\epsilon' = -\frac{Z''}{\omega * C_0(Z''^2 + Z'^2)} \quad (1)$$

One may get the imaginary component of the dielectric constant (ϵ'') by utilizing the following approach [24, 27, 28].

$$\epsilon'' = \frac{Z'}{\omega * C_0(Z''^2 + Z'^2)} \quad (2)$$

where Z' , Z'' , ω , and C_0 denote the real and imaginary components of impedance, angular frequency, and geometrical capacitance, respectively.

Frequency-dependent dielectric characterization

The frequency-dependent behavior of the real (ϵ') and imaginary (ϵ'') components of the dielectric constant for Mu-C00, Mu-C10, Mu-C20, and Mu-C30 ceramics sintered at 1600 °C for 1 h is analyzed across an extensive frequency spectrum

(100 Hz–1 MHz), (see Fig. 8). This behavior is reminiscent of that seen in other dielectric ceramics such as alumina, cordierite ($\text{Mg}_2\text{Al}_4\text{Si}_5\text{O}_{18}$), and perovskite ceramics like BaTiO_3 [29, 30]. The high dielectric constant observed at low frequencies in multiphase ceramics arises from multiple polarization mechanisms under an applied electric field, including ionic, dipolar (orientation), and electronic contributions. Among these, Maxwell–Wagner (interfacial) polarization plays a key role, explaining the frequency-dependent permittivity through charge accumulation at interfaces between different phases. In this frequency regime, dipolar polarization and space charge effects dominate, as defects, structural imperfections, and mobile ions facilitate localized charge buildup at grain boundaries or surfaces when subjected to an electric field.

Interfacial polarization primarily arises from conductivity differences among the constituent phases, such as cordierite, mullite, and the glassy matrix [31, 32]. Since grain boundaries hinder charge carrier movement across crystallites, electrons and ions accumulate at these interfaces, leading to localized space charge effects. This charge segregation enhances the material's overall dielectric constant, particularly at lower frequencies where interfacial contributions dominate.

Dipoles cannot orient themselves in the field direction in such short a timescale, and the charge carriers cannot react fast enough to the fast changes in the applied electric field at higher frequencies.

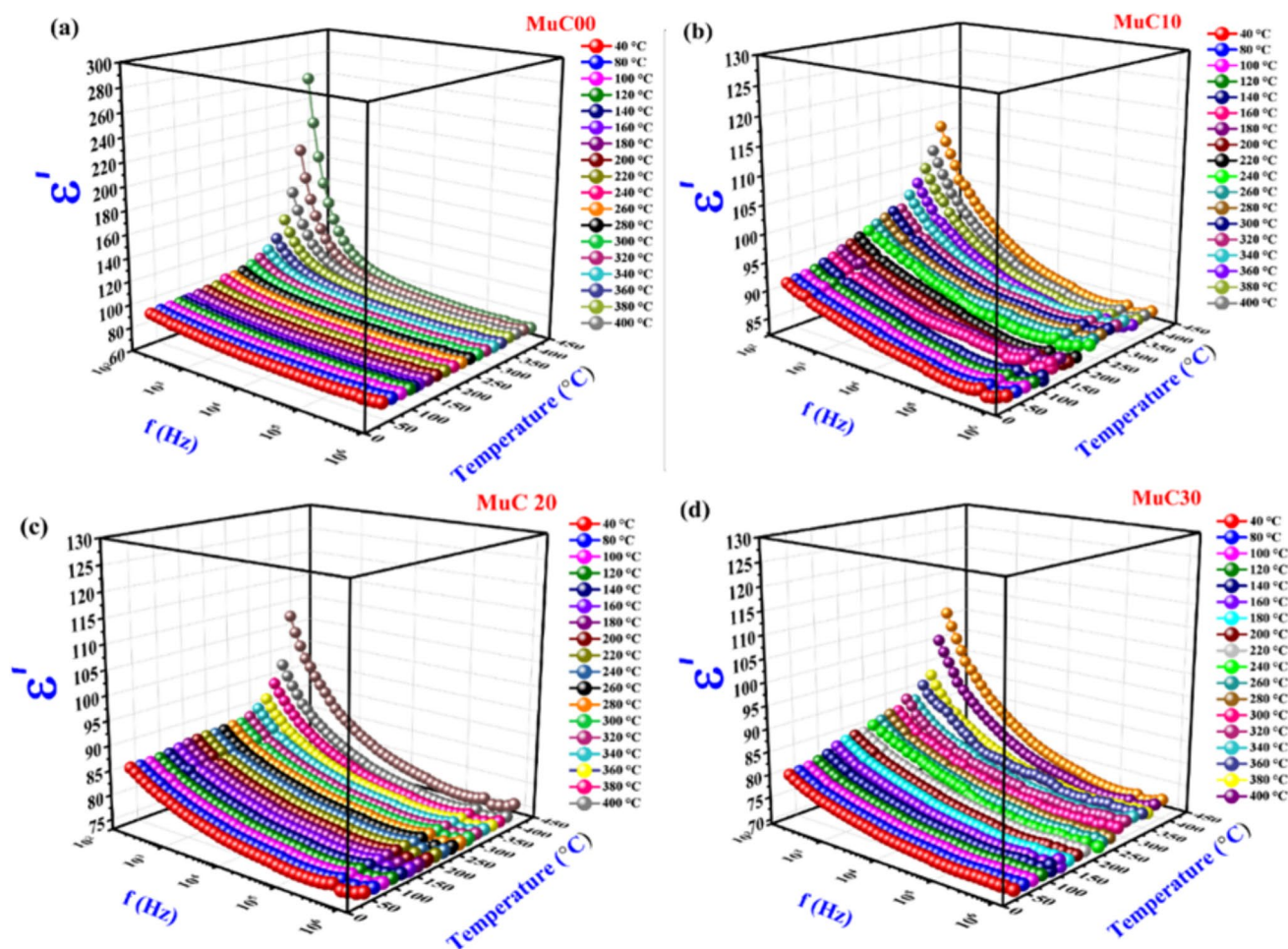


Figure 8 Variation of the real component (ϵ') of the dielectric constant with frequency for Mu-C00, Mu-C10, Mu-C20, and Mu-C30 ceramics.

Consequently, only electronic polarization adds to the dielectric constant at high frequencies, thereby reducing the dielectric constant with increasing frequency for both Mu-C00, Mu-C10, Mu-C20, and Mu-C30 (see Fig. 8).

Across the same frequency range (100 Hz–1 MHz), the dielectric imaginary component (ϵ'') was evaluated for the Mu-C00, Mu-C10, Mu-C20, and Mu-C30 ceramic samples.

Mu-C20 and Mu-C30 are also shown in the inset of Fig. 9. Ion hopping, ion/dipole polarization inside the material, and charge carrier migration all affect the imaginary (ϵ'') component of the dielectric constant at low frequencies. Dipoles become immobilized at high frequencies, however, and ion vibrations mostly contribute to the imaginary (ϵ'') component of the dielectric constant, thereby reducing ϵ' with increasing frequency [33, 34]. Still, in comparison with the

dielectric constant values of these ceramics, the value of ϵ'' is negligible.

Temperature-dependent dielectric analysis

The real (ϵ') and imaginary (ϵ'') components of the dielectric constant for Mu-C00, Mu-C10, Mu-C20, and Mu-C30 ceramics are depicted in Figs. 10a–d and 11a–d, respectively, across selected frequencies (10 Hz, 100 Hz, 1 kHz, 10 kHz, 100 kHz, and 1 MHz) within the temperature range of 40 °C to 400 °C. The dielectric property measurements were limited to 400 °C due to instrument constraints.

The non-dispersive behavior of the dielectric constant is evident in the plots of temperature versus the real (ϵ') and imaginary (ϵ'') components below 280 °C. The dielectric constant experiences

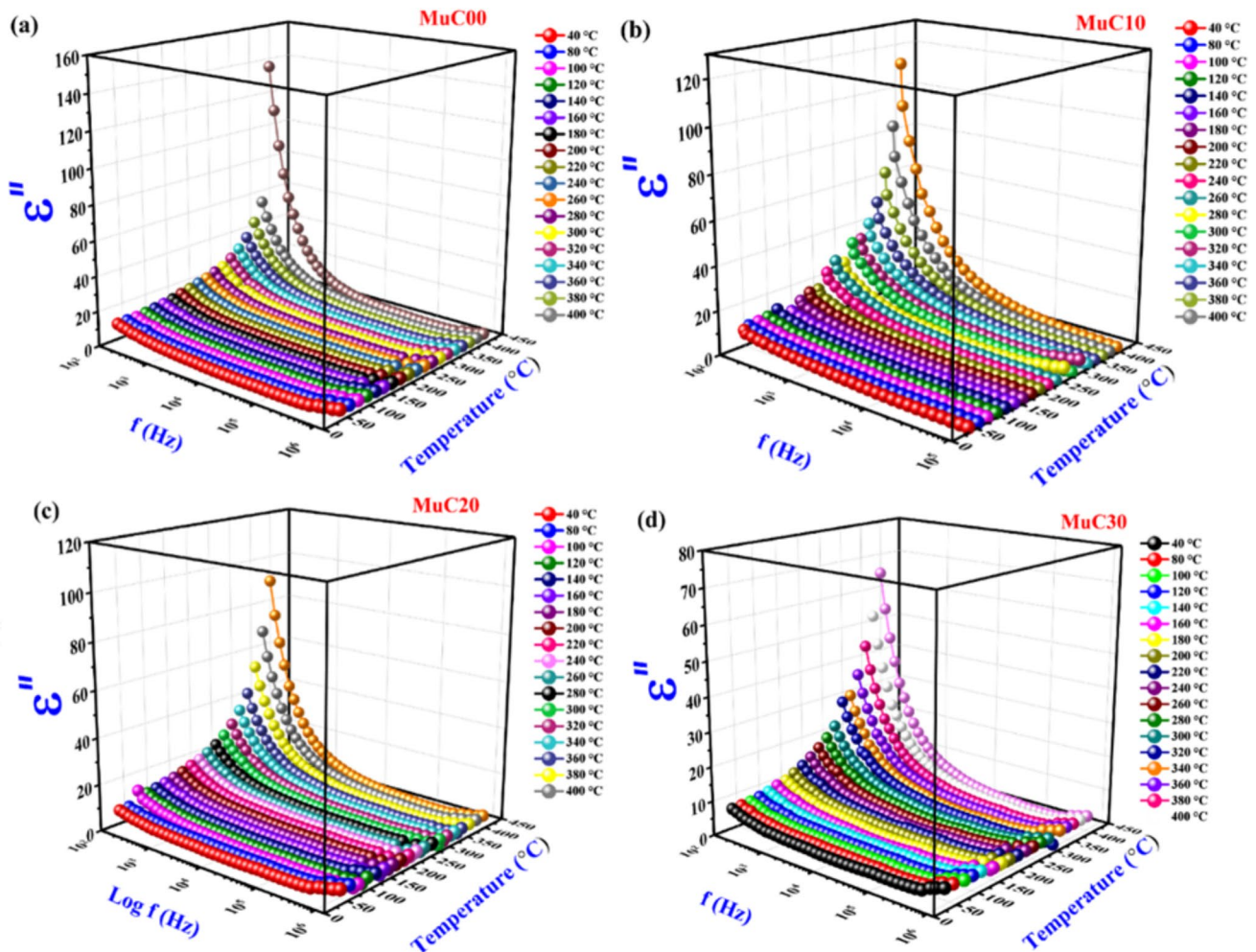


Figure 9 Variation of the imaginary component (ϵ'') of the dielectric constant with frequency for Mu-C00, Mu-C10, Mu-C20, and Mu-C30 ceramics.

a substantial increase in response to temperatures beyond 280 °C because of the enhanced temperature-dependent dipolar polarization. Electrical conduction increases as dipoles align more with increasing temperature, leading to an increase in both dielectric constant and dielectric loss values. However, initially, up to 100 °C for Mu-C00, Mu-C10, Mu-C20, and Mu-C30 ceramics, the dielectric constant shows a decreasing trend with temperature.

This can be attributed to the effect of heat on orientational polarization. At lower temperatures, molecules are in a frozen state with insufficient energy to overcome barriers, leading to a decrease in dielectric constant and loss. As the temperature rises further, dipoles gain sufficient energy to align along the electric field direction, progressively increasing the

quantities of the real (ϵ') and imaginary (ϵ'') components of the dielectric constant [35, 36].

Compositional dependence dielectric properties

Figures 12 and 13 demonstrate the modulation of the real (ϵ') and imaginary (ϵ'') components of the dielectric constant as a function of cordierite content at specific frequencies (10 Hz, 100 Hz, 1 kHz, 10 kHz, 100 kHz, and 1 MHz) and varying temperatures for (M/C Com.) sintered at 1600 °C for 1 h. The dielectric properties in this study were investigated at a sintering temperature of 1600 °C due to its capacity to attain greater densification. It is evident from the figures that the real (ϵ') and imaginary (ϵ'') components of the

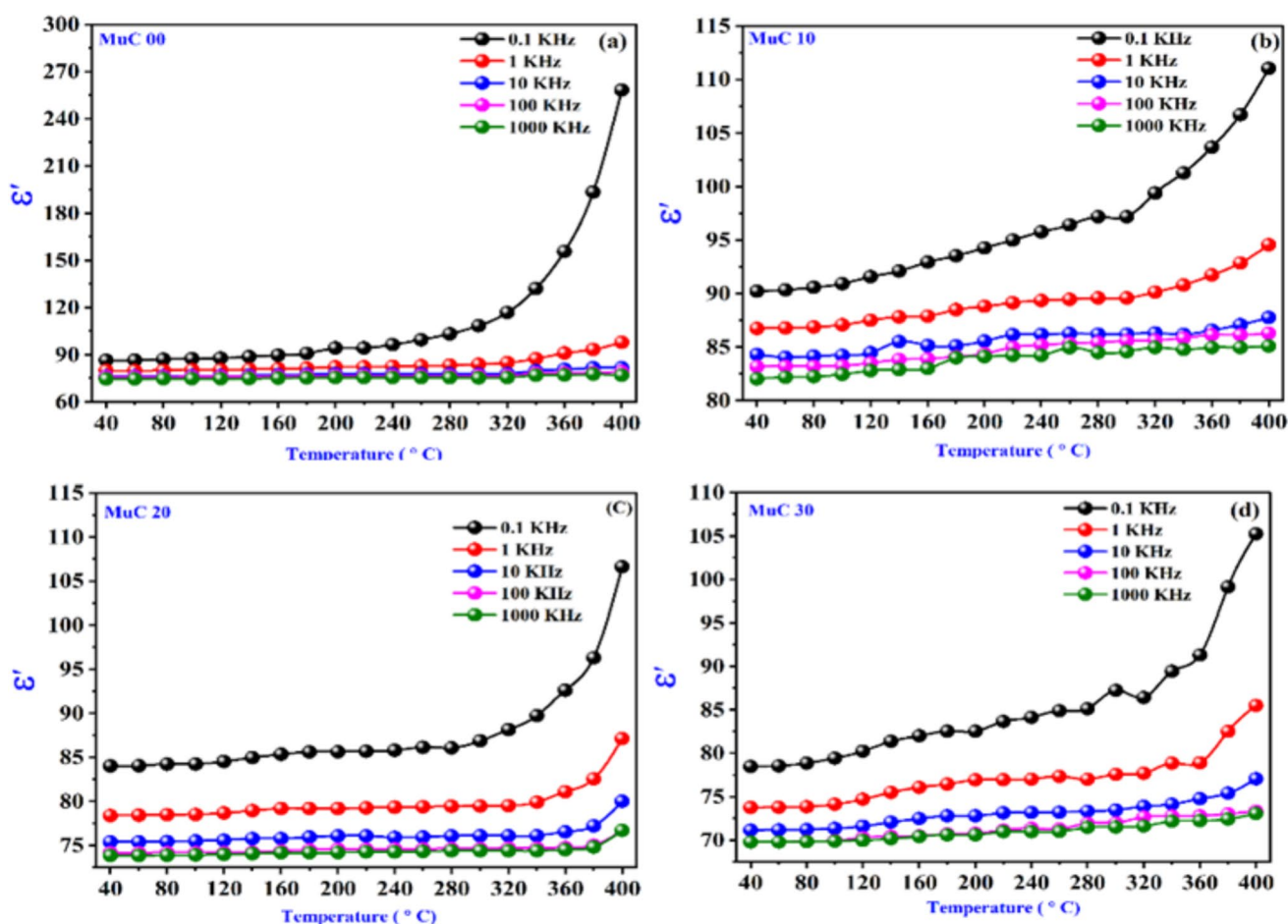


Figure 10 Change in the real component (ϵ') of the dielectric constant with temperature for Mu-C00, Mu-C10, Mu-C20, and Mu-C30 ceramics.

dielectric constant of the composites diminish as the proportion of cordierite increases. This is most likely due to the decreased porosity as the relative quantity of cordierite increased. Sample Mu-C30 exhibited the lowest values for both the real (ϵ') and imaginary (ϵ'') portions of the dielectric constant, with porosity values of 9.69. The dissolution of the cordierite phase in the mélange has resulted in the presence of a glass phase, which can be attributed to the reduction in porosity. This suggests that the porosity and processing conditions of the composite under investigation affect its dielectric behavior [37]. At temperatures exceeding 1600 °C, the predominance of mullite and vitreous phases resulted in a substantial decrease in porosity and a decrease in interfacial area (interfacial polarization) per unit volume. The real (ϵ') and imaginary (ϵ'') components of the dielectric constant were both influenced by these factors. This effect was apparent in all the formulations that were examined, despite

fluctuations in the vitreous phase. This underscores the fact that the predominant phases (mullite) were the primary contributors to the dielectric constant. The growth of mullite and cordierite crystals is facilitated by an increase in the sintering temperature, which also reduces the material's porosity, according to research findings [38–40]. The interfacial area per unit volume is reduced, consequently, which has a substantial impact on the material's dielectric constant. Minimizing the glass phase's presence in ceramic bodies is essential for achieving optimal dielectric performance, particularly at high frequencies, as it tends to reduce the dielectric constant [41].

AC conductivity studies

Conductivity assessments in alternating current (AC) play a vital role in studying the ionic transport

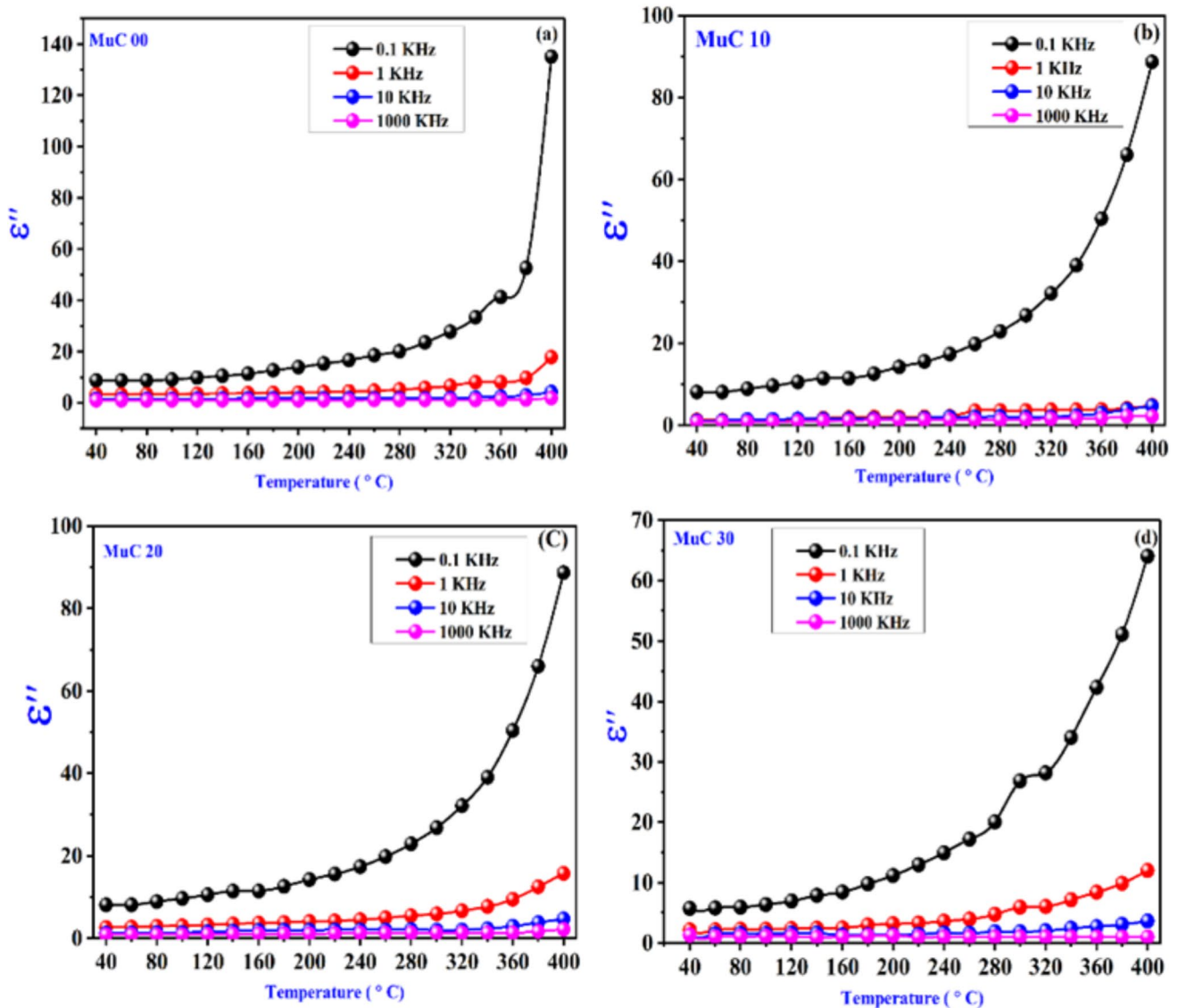


Figure 11 Fluctuations of the imaginary part (ϵ'') of the dielectric constant with temperature for Mu-C00, Mu-C10, Mu-C20, and Mu-C30 ceramics.

characteristics of materials. The AC conductivity data were obtained using the following expression [42–44];

$$\sigma_{AC} = \omega \cdot \epsilon'' \cdot \epsilon_0 = 2\pi f \cdot \epsilon'' \cdot \epsilon_0 \quad (3)$$

where f denotes the frequency of the applied field, ϵ'' represents the imaginary component of the dielectric constant, $\omega = 2\pi f$ is the angular frequency, and ϵ_0 is the permittivity of free space.

Figure 14 illustrates how the AC conductivity varies with frequency for Mu-C00, Mu-C10, Mu-C20, and Mu-C30 ceramics synthesized via the sol-gel technique and sintered at 1600 °C under diverse temperatures. It shows typical behavior observed in

ionic materials: conductivity remains constant (DC plateau) at low frequencies but rises as frequency increases. The characterization of conductivity dispersion often follows Jonscher's universal power law [5, 27, 45, 46].

$$\sigma_{AC} = \sigma_{DC} + A\omega^n \quad (4)$$

σ_{DC} represents the direct current (DC) conductivity, which is based on the frequency-independent plateau examined at low frequencies; A denotes a parameter influenced by temperature; and n indicates the frequency exponent related to mobile ions.

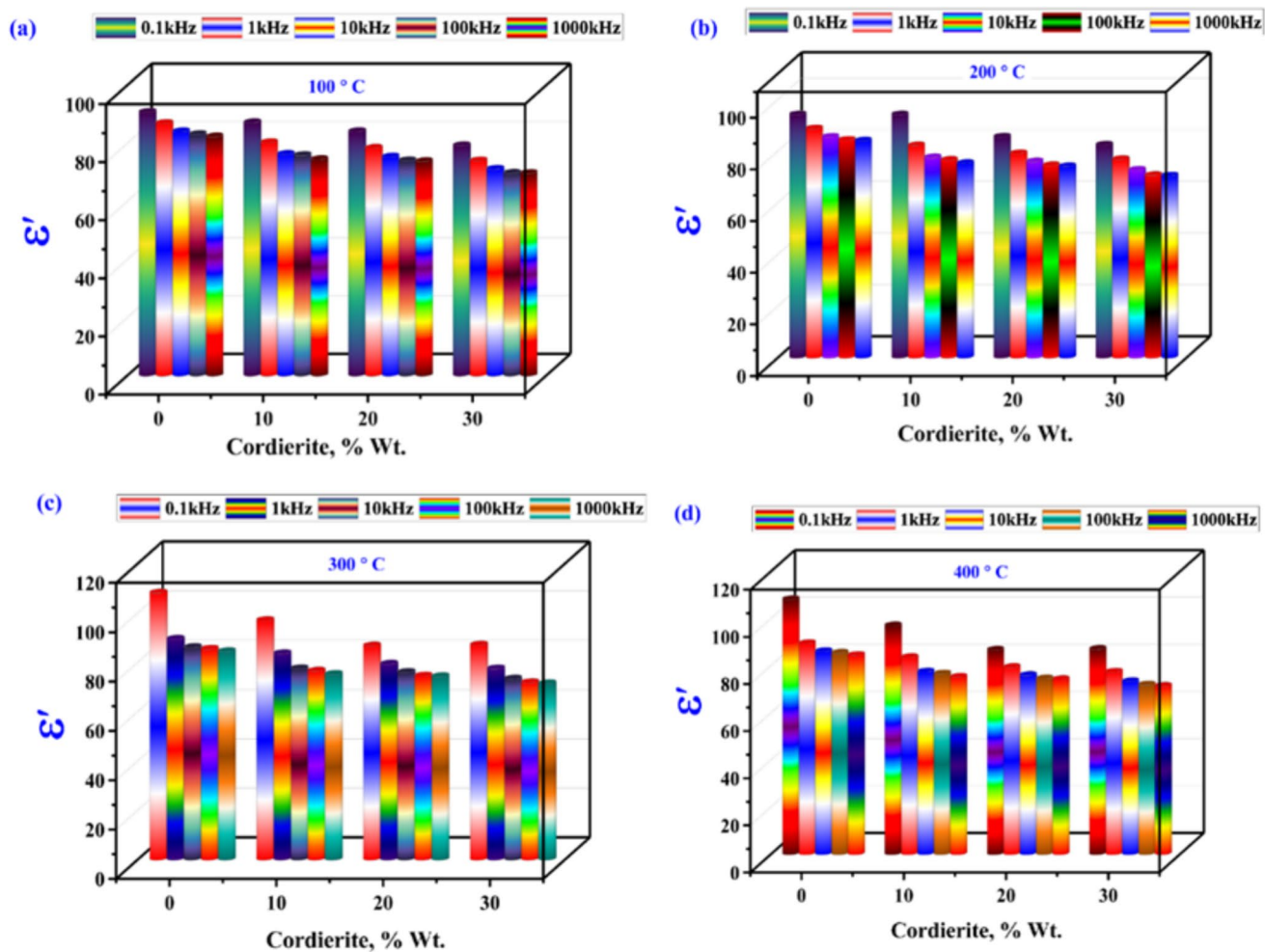


Figure 12 Imaginary (ϵ'') component of the dielectric constant changes with temperature for Mu-C00, Mu-C10, Mu-C20, and Mu-C30 ceramics.

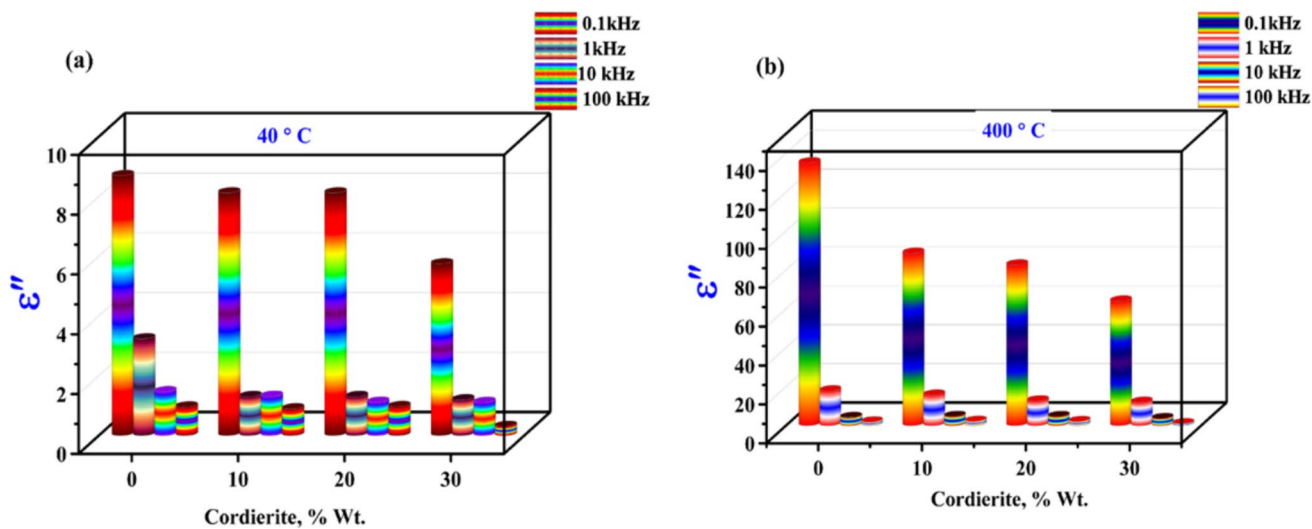


Figure 13 Imaginary (ϵ'') component of the dielectric constant varies with temperature for M/C C ceramics.

To determine the activation energy (E_a), the DC electrical conductivity (σ_{dc}), extracted from low-frequency measurements, was analyzed using the thermally activated Arrhenius relation (Eq. 5) [31]:

$$\sigma_{dc} = \sigma_0 \exp\left(\frac{-E_a}{k_B T}\right) \quad (5)$$

where σ_0 is a pre-exponential factor, k_B is the Boltzmann constant, and E_a gives activation energy.

Figure 14e–h presents the Arrhenius plots of $\ln(\sigma_{dc})$ versus $10^3/T$ for Mu-C00, Mu-C10, Mu-C20, and Mu-C30 ceramics, from which the activation energy (E_a) values were determined using the slope of each linear fit. The calculated E_a values for all mullite/cordierite composite ceramics, summarized in Table 5, align well with the findings reported by Ahcen et al. [35], confirming the consistency of the electrical conduction mechanism across these materials.

Impedance analysis

The change in the real part of impedance (Z') with frequency at various temperatures for Mu-C00, Mu-C10, Mu-C20, and Mu-C30 is illustrated in Fig. 15a–d, respectively. As frequency increases, the impedance decreases, which is consistent with the observed increase in AC conductivity as frequency increases. Space charge polarization is indicated by the spikes observed at lower frequencies in the Z' versus frequency curve. The Z' curves converge for all temperatures at higher frequencies (> 100 kHz), which suggests a relaxation process resulting from the discharge of space charges near particle boundaries [27, 46, 47]. It is important to note that Z' increases with temperature at lower frequencies (from room temperature to 150 °C) and then decreases at higher temperatures. According to this behavior, the ceramics exhibit positive temperature coefficient of resistance (PTCR) behavior up to 150 °C, which transitions to negative temperature coefficient of resistance (NTCR) behavior from 250 to 450 °C. The PTCR behavior is ascribed to the decreased ion hopping between adjacent sites as the temperature increases, a phenomenon that becomes more pronounced above 150 °C.

Figure 16a–d also illustrates the variation in the imaginary part of impedance (Z'') with frequency for Mu-C00, Mu-C10, Mu-C20, and Mu-C30 ceramics, respectively. Z'' decreases with increasing frequency at lower temperatures and becomes

frequency-independent beyond 100 kHz. Furthermore, peaks that correspond to Z'' max are observed at 350 °C and 450 °C for Mu-C00, Mu-C10, Mu-C20, and Mu-C30, respectively. These peaks begin to manifest at temperatures of 250 °C and higher. The electrical relaxation frequency is the frequency at which Z'' max peaks appear for a specific temperature, and the peak height is indicative of the bulk resistance of the material. These peaks become asymmetrically broadened and shift toward higher frequencies as the temperature increases, which is a characteristic of electrical relaxation phenomena with prolonged relaxation periods within the materials at high temperatures [48–51]. In contrast, the monotonic decrease in Z'' without a peak appearance at lower temperatures implies that relaxation phenomena in these materials are only present at elevated temperatures, where immobile defects in the material may function as relaxation species [52].

Nyquist curve

Nyquist plots ($-Z''$ vs. Z') for Mu-C00, Mu-C10, Mu-C20, and Mu-C30 ceramics are illustrated in Fig. 17. The transport properties of the material are elucidated by these graphs, which demonstrate the contributions of electrode interfaces, grain boundaries, and grains. In a manner similar to an equivalent RC circuit model, each contribution is depicted by semicircular arcs [53, 54]. The electrical relaxation phenomena within the dielectrics are reflected in the geometry of these arcs. Our synthesized ceramics exhibit depressed semicircles that are inclined toward the real impedance (Z') axis, as is typical of ceramics that exhibit non-Debye-type relaxation because of variations in particle size distribution and electromagnetic diffusion [55]. As the temperature rises, the semicircular arcs decrease in radius, suggesting a stronger influence of thermal effects on impedance behavior at higher temperatures and a decrease in total electrical resistance. This is consistent with the ceramics' negative temperature coefficient (NTC) behavior, which has been observed in high-temperature regions [27, 56]. The impedance spectrum exhibits virtually linear behavior at temperatures below 250 °C, suggesting that the ceramics have a higher grain boundary resistance. The combined effects of both grains and grain boundaries on impedance are confirmed by the appearance of semicircular arcs at elevated temperatures.

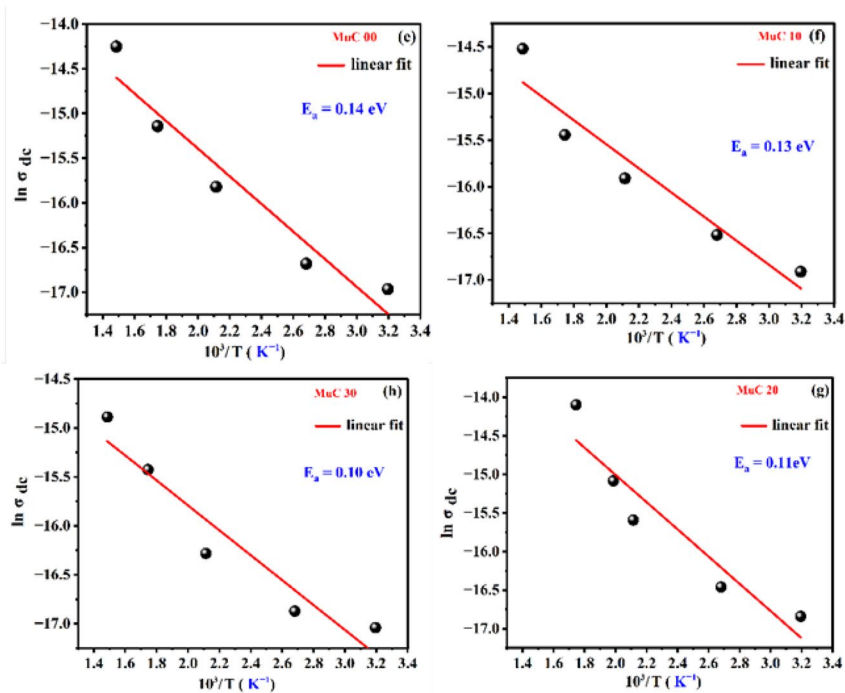
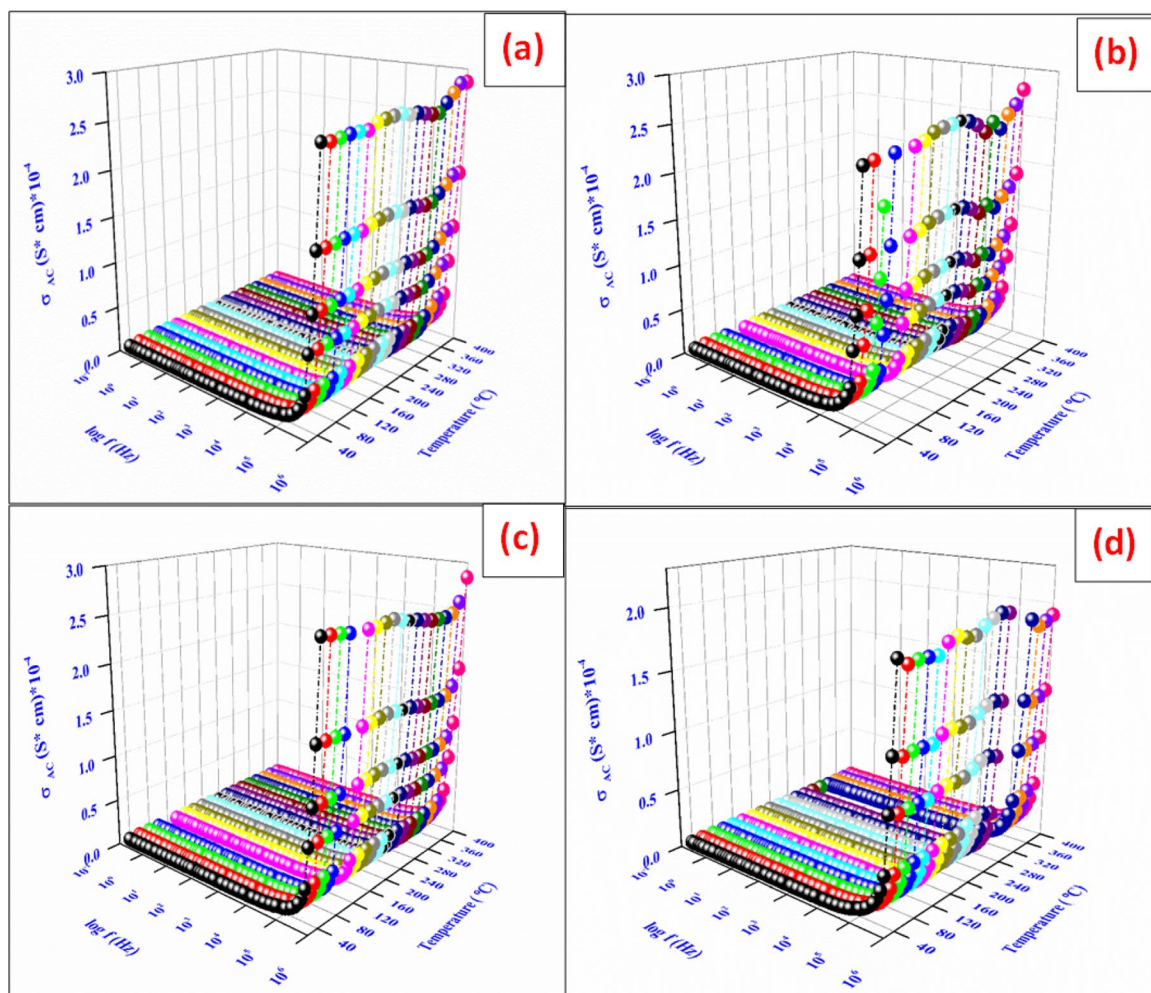


Figure 14 Changes in AC conductivity with both frequency and temperature for (M/C C) ceramics Variation of $\ln(\sigma_{dc}T)$ as a function of $10^3/T$ for (M/C C) ceramics.

Table 5 Activation energy values of mullite/cordierite composite ceramics

Mullite/ Cordierite composite	Activation energy (eV)
Mu-C00	0.14
Mu-C10	0.13
Mu-C20	0.11
Mu-C30	0.10

Complex modulus analysis

The electrical modulus can be precisely defined utilizing the equations provided in [56]:

$$M^* = M' + jM''$$

The following expressions were employed to calculate the real and imaginary components of the complex electrical modulus, as outlined in [57, 58].

$$M' = \frac{\epsilon'}{(\epsilon'^2 + \epsilon''^2)} \quad (6)$$

$$M'' = \frac{\epsilon''}{(\epsilon'^2 + \epsilon''^2)} \quad (7)$$

The M' versus frequency contours for Mu-C00, Mu-C10, Mu-C20, and Mu-C30 are illustrated in Fig. 18a–d at varying temperatures. The presence of multiple relaxation processes in these ceramics is suggested by the broad asymmetric peak that shifts toward higher frequencies as temperature increases [27, 59].

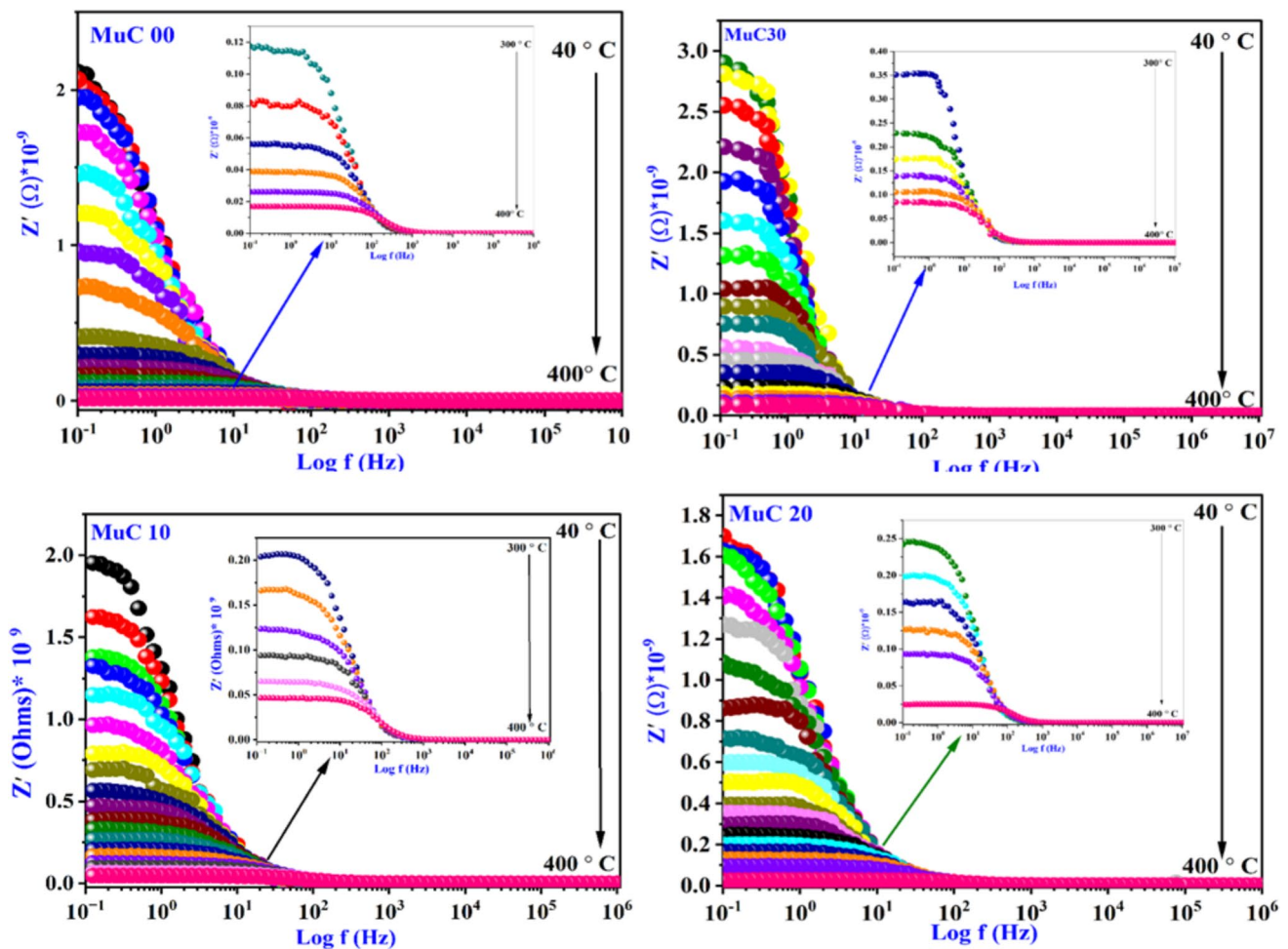


Figure 15 Real component of impedance (Z') changes across different frequencies and temperatures in composites made of mullite and cordierite for Mu-C00, Mu-C10, Mu-C20, and Mu-C30 ceramics.

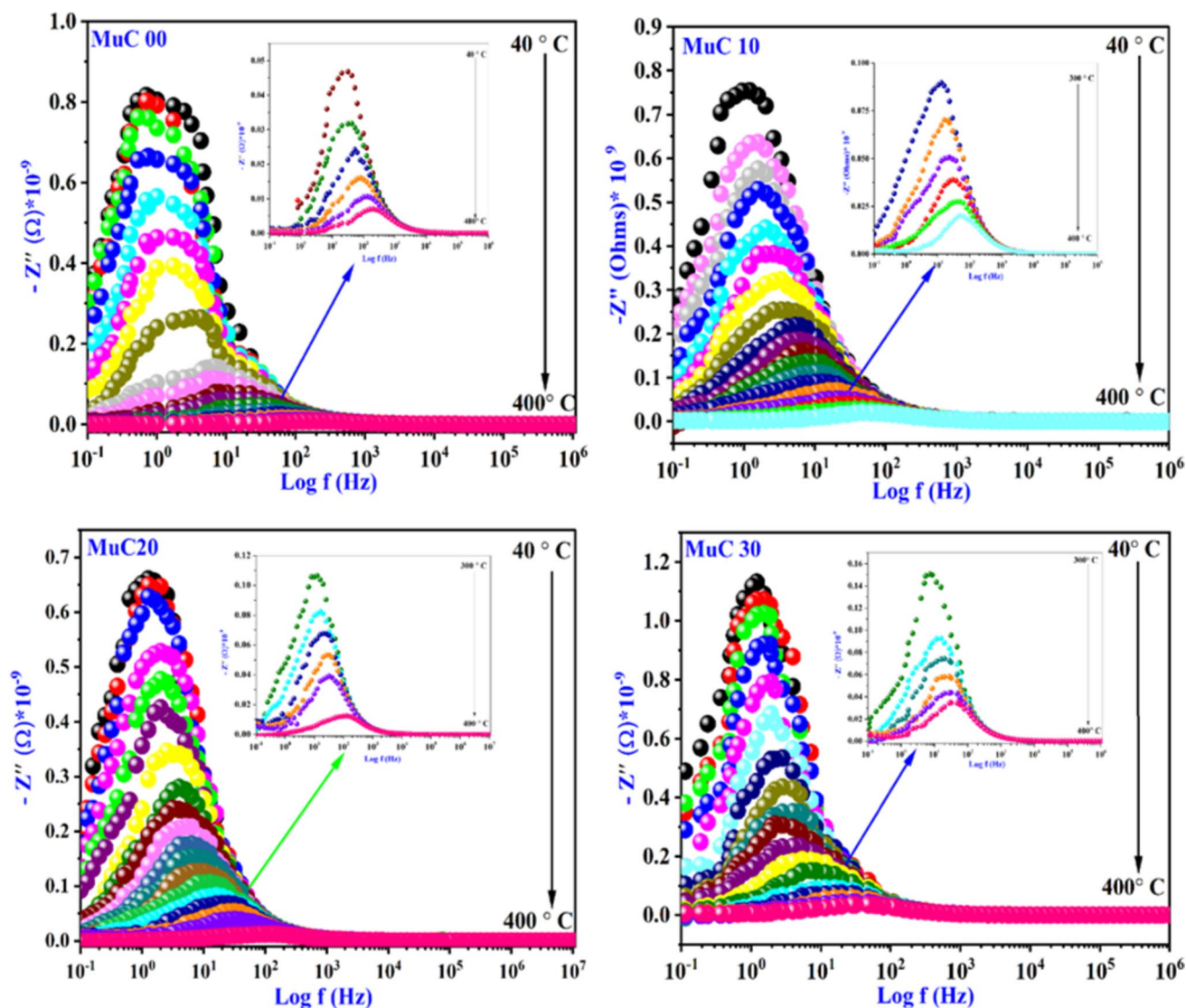


Figure 16 Changes in the imaginary component of impedance (Z'') across diverse frequencies and temperatures in composites consisting of mullite and cordierite for Mu-C00, Mu-C10, Mu-C20, and Mu-C30 ceramics.

Figure 19a–d illustrates the frequency dependence of M'' at varying temperatures for Mu-C00, Mu-C10, Mu-C20, and Mu-C30, respectively. The low-frequency side of these M'' curves exhibits peaks that migrate toward higher frequencies as the temperature increases. This behavior implies a transition from long-range to short-range motion of charge carriers or dipoles as the frequency increases. The high dielectric constant observed at this low frequency is a direct result of the exceedingly low value of M' (almost negative) at 100 Hz. Furthermore, the minimal electrode effects at low frequencies are suggested by the

convergence of M' values to a minimum value (close to zero) [60]. The modest positive temperature coefficient of resistance (PTCR) effect observed in these ceramics can be attributed to the anomalous increase in M'' values toward M_∞ [27, 61]. A discrepancy in the peak positions between Z'' and M'' curves is evident for both Mu-C00, Mu-C10, Mu-C20, and Mu-C30 ceramics, as shown in Fig. 20a–d. This behavior implies that charge carriers are moving in our samples at a short-range or localized level at the experimental temperature of 400 °C [27, 61]. The absence of overlapping between the Z'' and M'' peaks further suggests that our

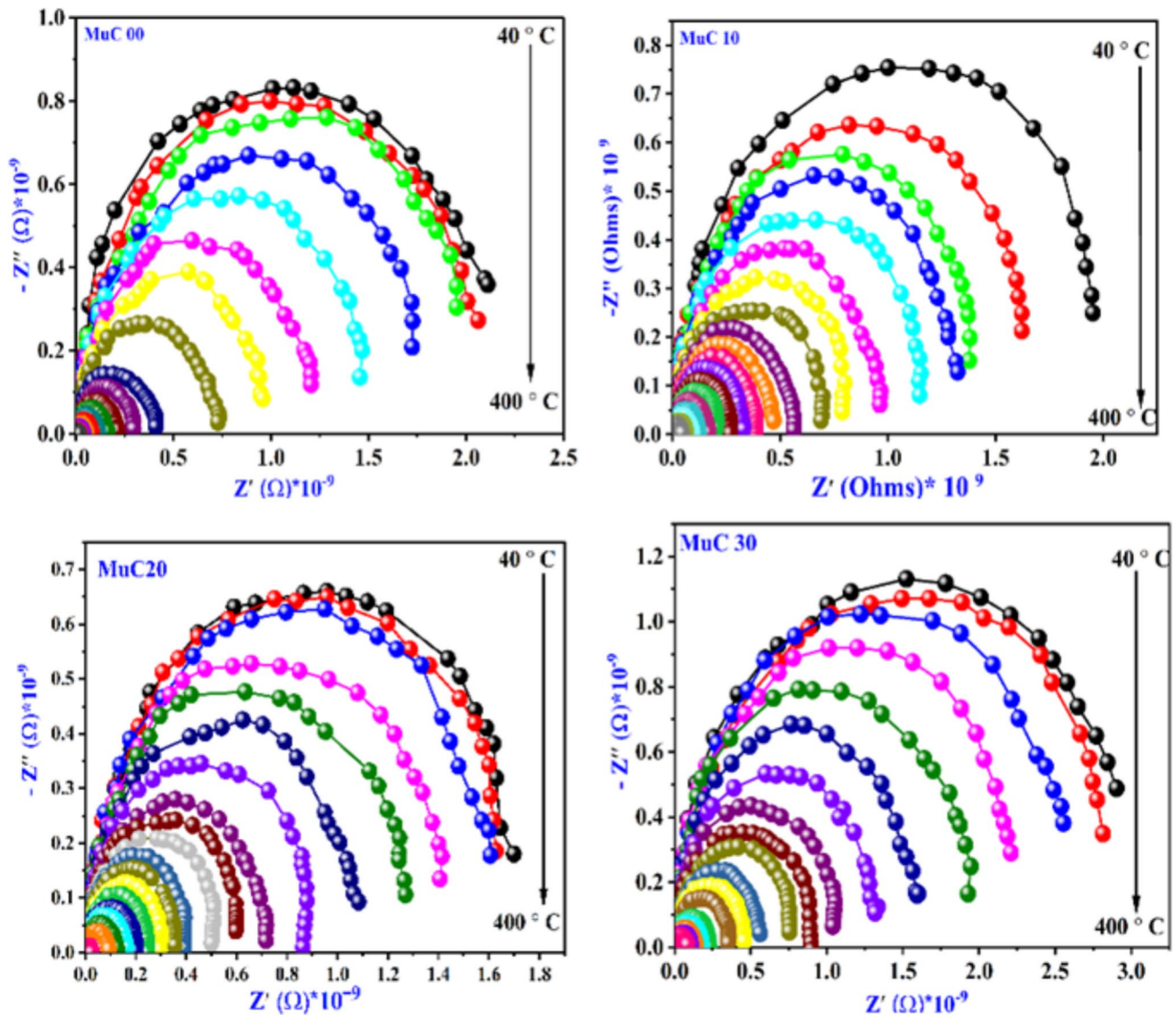


Figure 17 Nyquist curves ($-Z''$ vs. Z') for Mu-C00, Mu-C10, Mu-C20, and Mu-C30 ceramics.

ceramics deviate from the ideal Debye-type behavior [62].

Conclusions

A dense cordierite–mullite nanocomposite has been successfully obtained by a simple sol–gel method. All samples were sintered at 1600 °C for 1 h in order to study how the processing might influence the structure, microstructure, and dielectric properties of this kind of ceramic.

Based on the analysis, the Rietveld XRD diffraction structure development of the mullite/cordierite composite samples heated at 1600 °C demonstrates that the calculated and real-world data levels are very similar, indicating that the correct structures and starting factors were chosen for the tuning process. The Rietveld XRD analysis of mullite $\text{Al}_6\text{Si}_2\text{O}_{13}$ confirms its orthorhombic structure within the Pbam space group. Despite the low confidence factors, the suggested model closely fits the X-ray diffraction pattern of the mullite/cordierite mixtures. The results of the Rietveld refinement, including lattice parameters and reliability factors, support the validity of the adsorption process

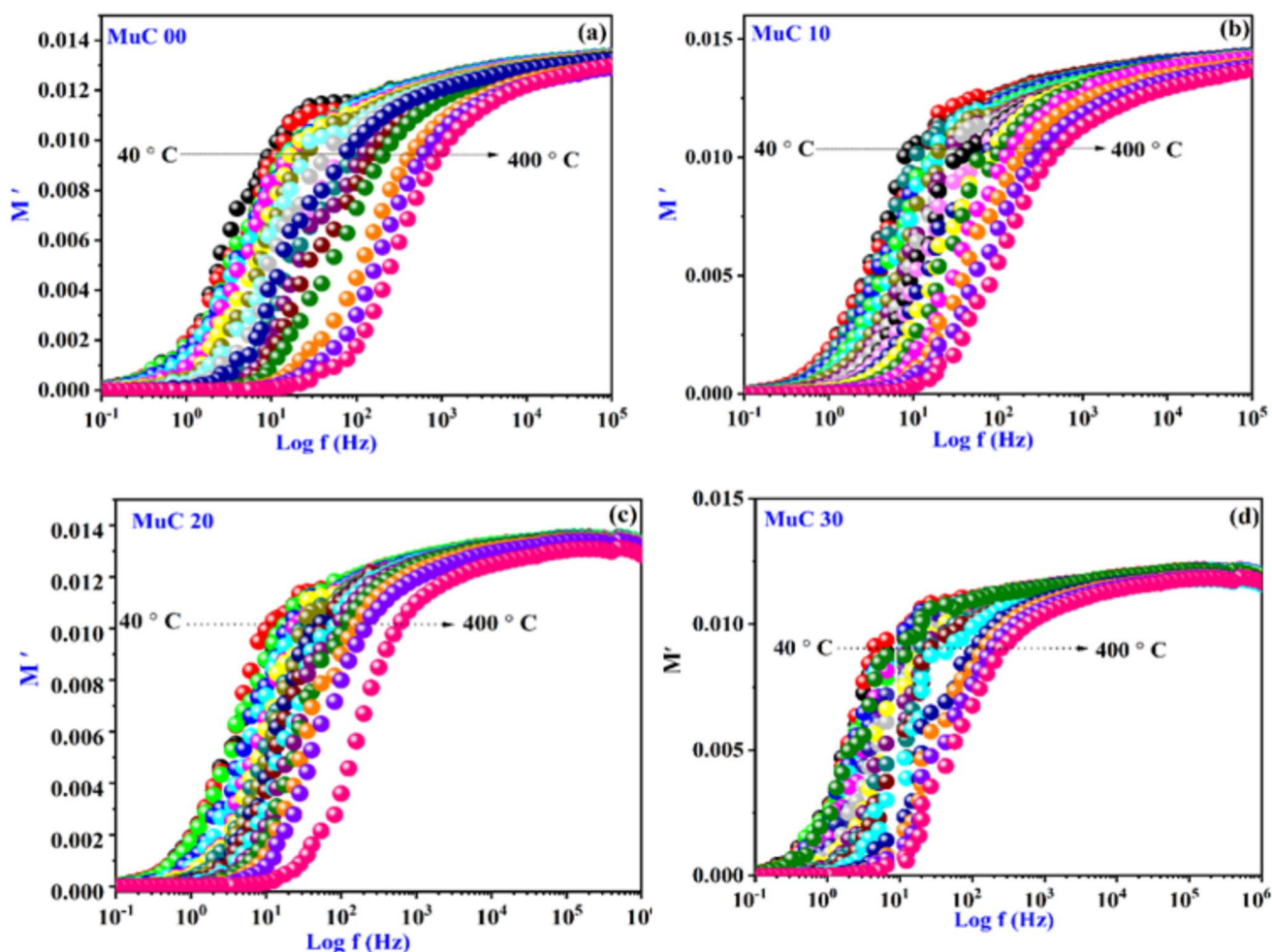


Figure 18 Real component of the electrical modulus for Mu-C00, Mu-C10, Mu-C20, and Mu-C30 ceramics.

and provide precise information on the structural parameters of the heat-treated samples.

The Mu-C30 sample prepared by the sol-gel method and treated at 1600 °C for 1 h presents a larger content of the glass phase, a lower grain size, and a more homogeneous distribution of crystals in the presence of the glassy phase. Moreover, Mu-C30 exhibits a lower porosity than Mu-C00, Mu-C10, and Mu-C20 samples. Temperature-dependent dielectric and the frequency-dependent behavior of the real (ϵ') and imaginary (ϵ'') parts of the dielectric constant for all samples was studied across a wide frequency range

(100 Hz – 1 MHz) and within the temperature range of 40 °C to 400 °C. The variation of the real (ϵ') and imaginary (ϵ'') parts of the dielectric constant as a function of cordierite content has been studied. The impedance and modulus analyses suggest the relaxation of space charges at the grain boundaries and the spreading of relaxation time with an increase in temperature. The Nyquist plots of both the mullite samples confirm the effect of both grain and grain boundary on the transport phenomena and the non-Debye-type relaxation mechanism in these samples.

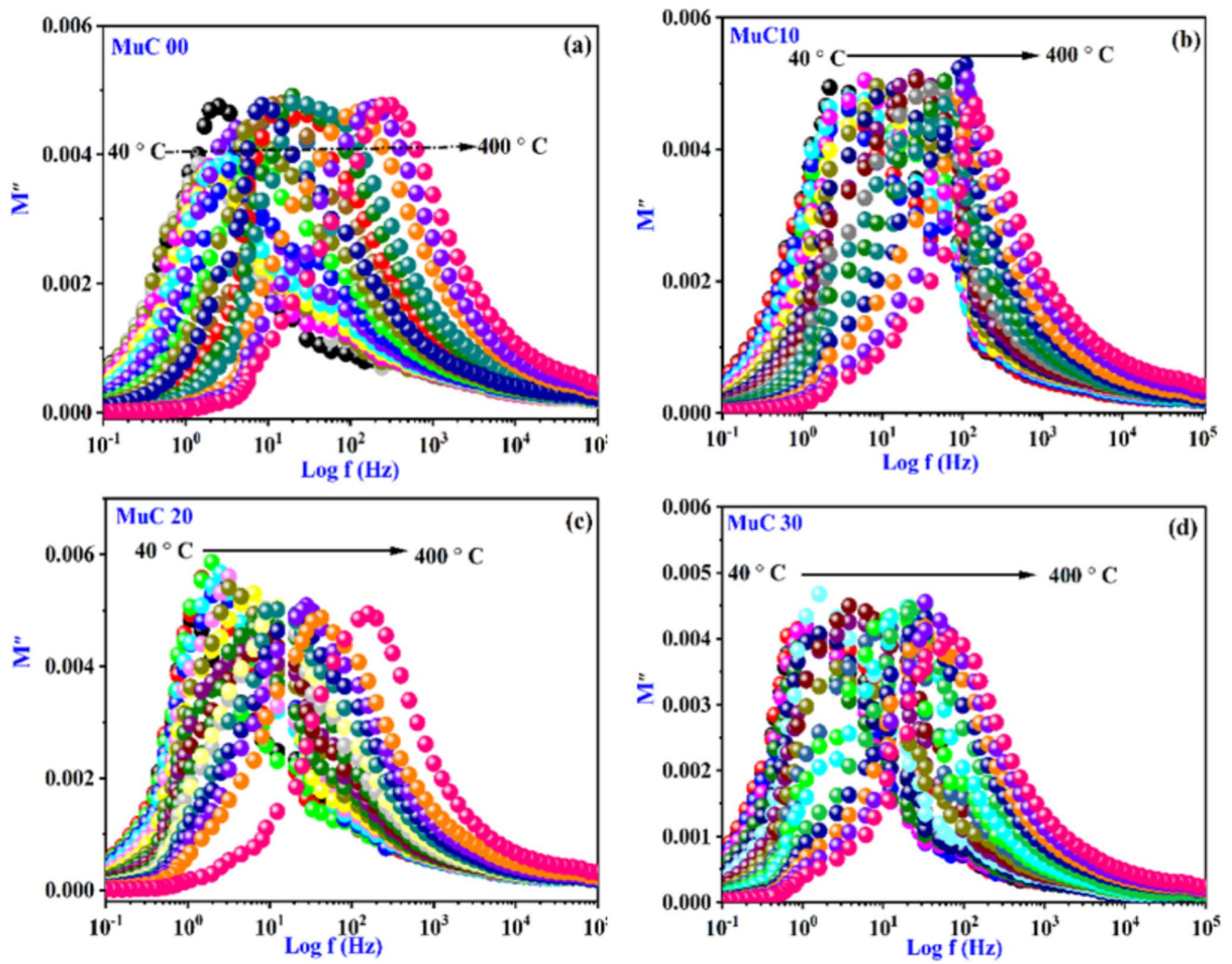


Figure 19 Imaginary component of the complex electrical modulus for Mu-C00, Mu-C10, Mu-C20, and Mu-C30 ceramics.

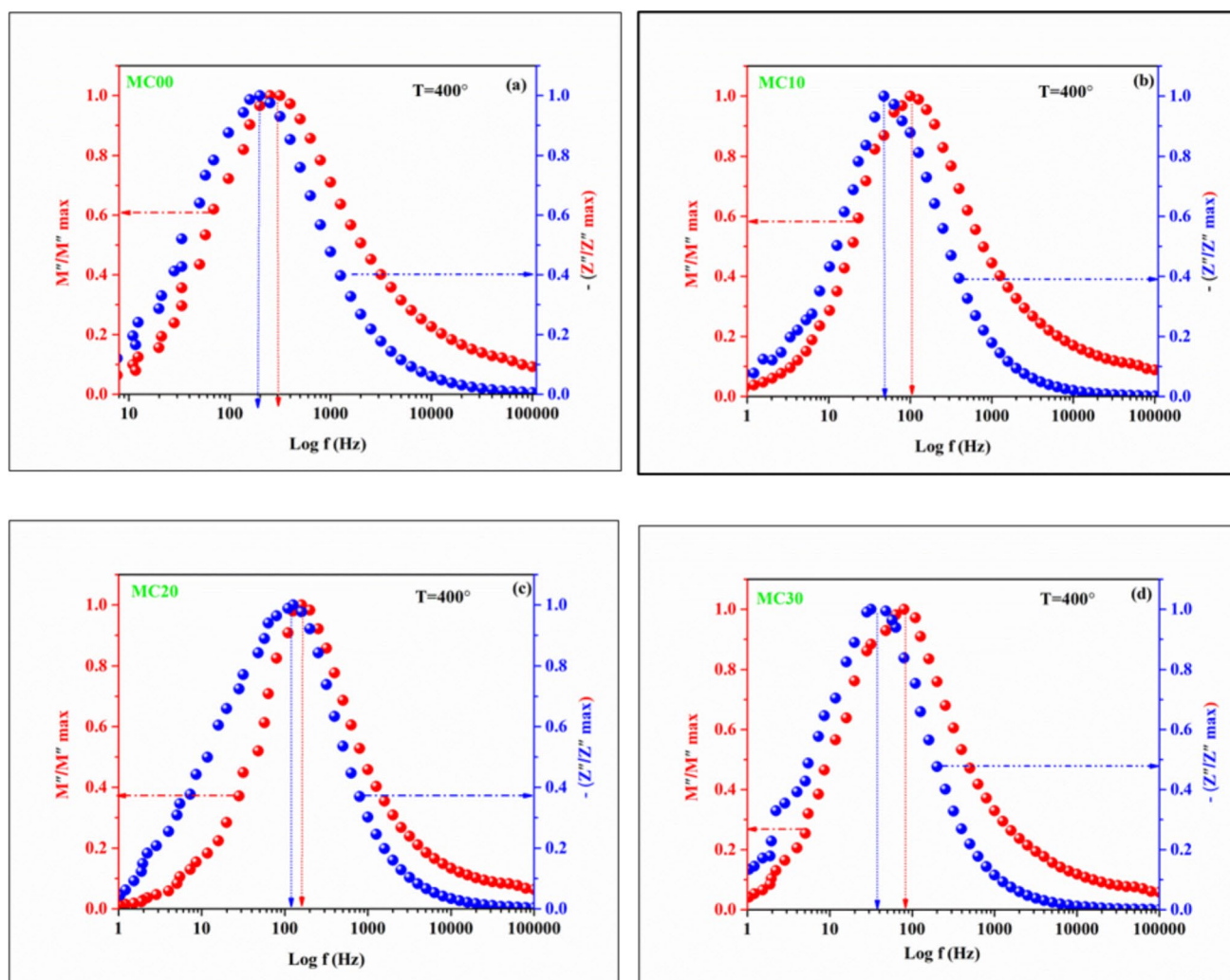


Figure 20 Frequency fluctuation of the M'' and $-Z''$ at 40 and 400 °C for Mu-C00, Mu-C10, Mu-C20, and Mu-C30 ceramics.

Acknowledgement

The authors are thankful for the computing resources of the Physics and Chemistry of Materials Laboratory University of M'sila in Algeria.

Author contributions

A. K., M. H., and M. R. assisted with methodology; A. O., M. R. and A. K. planned and conducted the tests, data analysis, and interpretation; A. K. and M. R. prepared the manuscript; and T.A.T revised and validated the final manuscript. All authors have read and approved the final manuscript version.

Funding

The authors have not disclosed any funding.

Data availability

On request, the corresponding author will provide you with the data sets generated during this investigation.

Declarations

Conflict of interest The authors declare that they have no known competing financial interests or per-

sonal relationships that could have appeared to influence the work reported in this paper.

Ethical approval Not applicable.

References

- [1] Keziz A, Heraiz M, Sahnoune F, Laziri K, Redaoui D, Saheb N (2023) Dense, hard, and thermally stable $\text{Al}_6\text{Si}_2\text{O}_{13}$ – $\text{Mg}_2\text{Al}_4\text{Si}_5\text{O}_{18}$ composite material for silicon substrate applications. *Silicon* 15(11):4675–4688. <https://doi.org/10.1007/s12633-023-02373-y>
- [2] Tulyaganov DU, Reddy AA, Kharton VV, Ferreira JMF (2013) Aluminosilicate-based sealants for SOFCs and other electrochemical applications - a brief review. *J Power Sources* 242:486–502. <https://doi.org/10.1016/j.jpowsour.2013.05.099>
- [3] Fuertes V, Cabrera MJ, Seores J, Muñoz D, Fernández JF, Enríquez E (2018) Hierarchical micro-nanostructured albite-based glass-ceramic for high dielectric strength insulators. *J Eur Ceram Soc* 38(7):2759–2766. <https://doi.org/10.1016/j.jeurceramsoc.2018.02.009>
- [4] Camerucci MA, Urretavizcaya G, Castro MS, Cavalieri AL (2001) Electrical properties and thermal expansion of cordierite and cordierite-mullite materials. *J Eur Ceram Soc* 21(16):2917–2923. [https://doi.org/10.1016/s0955-2219\(01\)00219-9](https://doi.org/10.1016/s0955-2219(01)00219-9)
- [5] Keziz A, Heraiz M, Sahnoune F, Rasheed M (2023) Characterization and mechanisms of the phase's formation evolution in sol-gel derived mullite/cordierite composite. *Ceramics Int* 49(20):32989–33003. <https://doi.org/10.1016/j.ceramint.2023.07.275>
- [6] Gao X et al (2023) Effect of micro/nano La_2O_3 addition on the sintering and properties of mullite synthesized. *Int J Appl Ceram Technol* 21(1):51–61. <https://doi.org/10.1111/ijac.14486>
- [7] Zhang B, Cao C, Zhu H, Li G (2005) Preparation low dielectric constant material of cordierite with polyacrylamide gel method. *J Mater Sci* 40:1781–1783. <https://doi.org/10.1007/s10853-005-0693-9>
- [8] Grilo JPF, Alves HPA, Araújo AJM, Andrade RM, Dutra RPS, Macedo DA (2019) Dielectric and electrical properties of a mullite/glass composite from a kaolinite clay/mica-rich kaolin waste mixture. *Ceramica* 65:117–121. <https://doi.org/10.1590/0366-69132019653732648>
- [9] Aksay IA, Dabbs DM, Sarikaya M (1991) Mullite for structural, electronic, and optical applications. *J Am Ceram Soc* 74(10):2343–2358. <https://doi.org/10.1111/j.1151-2916.1991.tb06768.x>
- [10] Kalendova A, Kupkova J, Urbaskova M, Merinska D (2024) Applications of clays in nanocomposites and ceramics. *Minerals* 14(1):93–93. <https://doi.org/10.3390/min14010093>
- [11] Lin X et al (2022) Analysis of unconventional boron-aluminum anomaly induced by mixed alkaline earth effect in glass substrate. *Mater Chem Phys* 282(801):125973–126015. <https://doi.org/10.1016/j.matchemphys.2022.125973>
- [12] Camerucci MA, Urretavizcaya G, Cavalieri AL (2001) Mechanical behavior of cordierite and cordierite–mullite materials evaluated by indentation techniques. *J Eur Ceram Soc* 21(9):1195–1204. [https://doi.org/10.1016/s0955-2219\(00\)00334-4](https://doi.org/10.1016/s0955-2219(00)00334-4)
- [13] Mei S, Yang J, Ferreira JMF (2001) Cordierite-based glass-ceramics processed by slip casting. *J Eur Ceram Soc* 21(2):185–193. [https://doi.org/10.1016/s0955-2219\(00\)00200-4](https://doi.org/10.1016/s0955-2219(00)00200-4)
- [14] Ahcen Keziz M, Rasheed M, Heraiz FS, Latif A (2023) Structural, morphological, dielectric properties, impedance spectroscopy and electrical modulus of sintered $\text{Al}_6\text{Si}_2\text{O}_{13}$ – $\text{Mg}_2\text{Al}_4\text{Si}_5\text{O}_{18}$ composite for electronic applications. *Ceramics Int* 49(23):37423–37434. <https://doi.org/10.1016/j.ceramint.2023.09.068>
- [15] Silva JN, Gonçalves PH, Chibério PH, Acchar W, Gomes UU (2016) The influence of microstructure, temperature and sintering level on electric properties of electrical insulators obtained from raw materials of Rio Grande do Norte - Brazil. *Mater Sci Forum* 881:111–116. <https://doi.org/10.4028/www.scientific.net/msf.881.111>
- [16] Tummala RR (1991) Ceramic and glass-ceramic packaging in the 1990s. *J Am Ceram Soc* 74(5):895–908. <https://doi.org/10.1111/j.1151-2916.1991.tb04320.x>
- [17] Li DX, Thomson WW (1990) Mullite formation kinetics of a single-phase gel. *J Am Ceram Soc* 73(4):964–969. <https://doi.org/10.1111/j.1151-2916.1990.tb05144.x>
- [18] Godbole K, Bhushan B, Narayana Murty SVS, Mondal K (2024) Al-Si controlled expansion alloys for electronic packaging applications. *Prog Mater Sci* 144:101268. <https://doi.org/10.1016/j.pmatsci.2024.101268>
- [19] Ismail U, Tsunatori H, Nakai Z (1990) Preparation of mullite cordierite composite powders by the sol-gel method: its characteristics and sintering. *J Am Ceram Soc* 73(3):537–543. <https://doi.org/10.1111/j.1151-2916.1990.tb06550.x>
- [20] Sembiring S, Simanjuntak W, Manurung P, Asmi D, Low IM (2014) Synthesis and characterisation of gel-derived mullite precursors from rice husk silica. *Ceram Int* 40(5):7067–7072. <https://doi.org/10.1016/j.ceramint.2013.12.038>

- [21] Chandran RG, Patil KC, Chandrappa GT (1995) Combustion synthesis, characterization, sintering and microstructure of mullite-cordierite composites. *J Mater Sci Lett* 14:548–551. <https://doi.org/10.1007/bf00275372>
- [22] Suzuki H, Saito H (1988) Preparation of precursor powders of cordierite-mullite composites from metal alkoxides and its sintering. *J Ceram Soc Japan* 96(1114):659–665. <https://doi.org/10.2109/jcersj.96.659>
- [23] Xu X, Zhang Y, Wu J, Hu C, Tang Z (2016) Preparation and performance study of cordierite/mullite composite ceramics for solar thermal energy storage. *Int J Appl Ceram Technol* 14(2):162–172. <https://doi.org/10.1111/ijac.12626>
- [24] El-Buaishi Nozhat Moftah, Janković-Častvan Ivona, Jokić Bojan, Veljović Djordje, Janačković Djordje, Petrović Rada (2012) Crystallization behavior and sintering of cordierite synthesized by an aqueous sol–gel route. *Ceramics Int* 38(3):1835–1841. <https://doi.org/10.1016/j.ceramint.2011.10.008>
- [25] López-Cuevas J, Interrial-Orejón E, Gutiérrez-Chavarría CA, Rendón-Ángeles JC (2017) Synthesis and characterization of cordierite, mullite and cordierite-mullite ceramic materials using coal fly ash as raw material. *MRS Adv* 2(62):3865–3872. <https://doi.org/10.1557/adv.2018.3>
- [26] Long L, Zhang Y, Zhu H, Li Y, Zhou W (2024) Multiple relaxation behavior of C/mullite composites and their electromagnetic wave performance at high temperatures. *Ceram Int*. <https://doi.org/10.1016/j.ceramint.2024.04.298>
- [27] Aryal S, Rulis P, Ching W (2012) Mechanical properties and electronic structure of mullite phases using first-principles modeling. *J Am Ceram Soc* 95(7):2075–2088. <https://doi.org/10.1111/j.1551-2916.2012.05172.x>
- [28] Abbas R, Abdelzaher MA, Shehata N, Tantawy MA (2024) Production, characterization and performance of green geopolymer modified with industrial by-products. *Sci Rep* 14(1):5104. <https://doi.org/10.1038/s41598-024-55494-8>
- [29] Li J-H, Wang S-F, Hsu Y-F, Chung T-F, Yang J-R (2018) Effects of Sc_2O_3 and MgO additions on the dielectric properties of BaTiO_3 -based X8R materials. *J Alloys Compd* 768:122–129. <https://doi.org/10.1016/j.jallcom.2018.07.196>
- [30] Wang B et al (2023) Effect of B4C particle size and TiB_2 content on the mechanical properties of B4C composites and their dynamic mechanical properties. *Int J Appl Ceram Technol* 21(1):438–450. <https://doi.org/10.1111/ijac.14522>
- [31] Ntholeng N, Rokebrand P, Mphasha NP, Sigalas I (2023) Properties of porous mullite filter material fabricated from reaction sintered mullite grains. *J Mater Eng Perform*. <https://doi.org/10.1007/s11665-023-08462-8>
- [32] Abdelzaher MA, Farghali AA, Hamouda AS (2024) Effective impact of nano-plastic-waste incorporated with nanotitina on the physical, mechanical and microstructural properties of white cement pastes composites for progressing towards sustainability. *Sci Rep* 14(1):12581. <https://doi.org/10.1038/s41598-024-62661-4>
- [33] Bochenek D et al (2024) Magnetoelectric properties of multiferroic composites based on BaTiO_3 and nickel-zinc ferrite material. *Materials (Basel)* 17(8):1905. <https://doi.org/10.3390/ma17081905>
- [34] Yang X et al (2024) Grain size effect of the flexoelectric response in BaTiO_3 ceramics. *J Appl Phys*. <https://doi.org/10.1063/5.0186230>
- [35] Keziz Ahcen, Meand Heraiz M. Rasheed, Oueslati Abderazek (2024) Investigating the dielectric characteristics, electrical conduction mechanisms, morphology, and structural features of mullite via sol-gel synthesis at low temperatures. *Mater Chem Phys*. <https://doi.org/10.1016/j.matchemphys.2024.129757>
- [36] Majumder SB, Bhattacharyya S, Katiyar RS, Manivannan A, Dutta P, Seehra MS (2006) Dielectric and magnetic properties of sol-gel-derived lead iron niobate ceramics. *J Appl Phys* 99(2):024108–024108. <https://doi.org/10.1063/1.2158131>
- [37] Kool A, Thakur P, Bagchi B, Hoque NA, Banerjee S, Das S (2015) Sol–gel synthesis of transition-metal ion conjugated alumina-rich mullite nanocomposites with potential mechanical, dielectric and photoluminescence properties. *RSC Adv* 5(126):104299–104313. <https://doi.org/10.1039/c5ra21091g>
- [38] Olabi AG, Shehata N, Issa UH, Mohamed OA, Mahmoud M, Abdelkareem MA, Abdelzaher MA (2025) The role of green buildings in achieving the sustainable development goals. *Int J Thermofluids* 25:101002. <https://doi.org/10.1016/j.ijft.2024.101002>
- [39] Belhouchet K, Bayadi A, Belhouchet H, Romero M (2019) Improvement of mechanical and dielectric properties of porcelain insulators using economic raw materials. *Boletín de la Sociedad Española de Cerámica y Vidrio* 58(1):28–37. <https://doi.org/10.1016/j.bsecv.2018.05.004>
- [40] Carvalho RS, da Silva B, Lira HL, Santana LNL (2020) Fabrication and characterization of dielectric ceramics using alumina and aluminosilicates. *Cerâmica* 66(377):56–64. <https://doi.org/10.1590/0366-69132020663772808>
- [41] Abdelzaher MA (2023) Sustainable development goals for industry, innovation, and infrastructure: demolition waste incorporated with nanoplastic waste enhanced the physico-mechanical properties of white cement paste composites. *Appl Nanosci* 13:5521–5536. <https://doi.org/10.1007/s13204-023-02766-w>
- [42] Rastgoo N, Darvishian Haghighi F, Haddad Sabzevar M, Mollazadeh Beidokhti S (2024) Aluminosilicate

- bioglass-ceramics: investigation of the crystallization trend through kinetic calculation and experimental study. *J Aust Ceram Soc.* <https://doi.org/10.1007/s41779-024-00998-9>
- [43] Ghosh B, Bhattacharya D, Raychaudhuri AK, Arumugam S (2009) Frequency dependence of dielectric anomaly around Néel temperature in bilayer manganite $\text{Pr}(\text{Sr}_{0.1}\text{Ca}_{0.9})_2\text{Mn}_2\text{O}_7$. *J Appl Phys.* <https://doi.org/10.1063/1.3153124>
- [44] Ouachou NL, Es-soufi H, Sayyed MI, Ghyati S, Bih L (2023) Investigation of structural, thermal, and electrical characteristics of zirconium-doped lithium-phosphate glasses. *Heliyon* 9(9):1–17. <https://doi.org/10.1016/j.heliyon.2023.e19364>
- [45] Xiao DQ et al (2016) Modification of optical and electrical properties of sol-gel-derived TiO_2 -doped ZrO_2 gate dielectrics by annealing temperature. *J Alloy Compd* 688:252–259. <https://doi.org/10.1016/j.jallcom.2016.07.179>
- [46] Abbas R, Shehata N, Mohamed EA, Salah H, Abdelzaher M (2021) Environmental safe disposal of cement kiln dust for the production of geopolymers. *Egypt J Chem* 64(12):7529–7537. <https://doi.org/10.21608/ejchem.2021.89060.4276>
- [47] Sharma S, Siqueiros JM, Srinet G, Kumar S, Prajapati B, Dwivedi R (2018) Structural, electrical, optical and dielectric properties of sol-gel derived $(1-x)\text{BiFeO}_3-(x)\text{Pb}(\text{Zr}_{0.52}\text{Ti}_{0.48})\text{O}_3$ novel multiferroics materials. *J Alloys Compd* 732:666–673. <https://doi.org/10.1016/j.jallcom.2017.10.144>
- [48] Kherifi Djelil, Ahcen Keziz M, Rasheed Abderrazek Oueslati (2024) Thermal treatment effects on Algerian natural phosphate bioceramics: a comprehensive analysis. *Ceramics Int.* <https://doi.org/10.1016/j.ceramint.2024.05.317>
- [49] Sarangi S, Badapanda T, Behera B, Anwar S (2013) Frequency and temperature dependence dielectric behavior of barium zirconate titanate nanocrystalline powder obtained by mechanochemical synthesis. *J Mater Sci Mater Electron* 24:4033–4042. <https://doi.org/10.1007/s10854-013-1358-0>
- [50] Shui X, Zou C, Zhang W, Bao C, Huang Y (2021) Effect of M^{3+} ($\text{M} = \text{Bi}, \text{Al}$) co-doping on the luminescence enhancement of $\text{Ca}_2\text{ZnSi}_2\text{O}_7: \text{Sm}^{3+}$ orange-red-emitting phosphors. *Ceram Int* 47(6):8228–8235. <https://doi.org/10.1016/j.ceramint.2020.11.182>
- [51] Ghosh J, Ali MS, Bhattacharya S (2024) Dielectric relaxation and AC conductivity of Fe-doped glassy semiconductors: role of Fe doping on relaxation time. *ECS J Solid State Sci Technol.* <https://doi.org/10.1149/2162-8777/ad2b9e>
- [52] Youness RA, Al-Ashkar E, Taha MA (2023) Role of porosity in the strength, dielectric properties, and bioactivity of hardystonite ceramic material for use in bone tissue engineering applications. *Ceram Int* 49(24):40520–40531. <https://doi.org/10.1016/j.ceramint.2023.10.029>
- [53] Kadri E et al (2017) Optical and electrical properties of SiGe/Si solar cell heterostructures: ellipsometric study. *J Alloy Compd* 721:779–783. <https://doi.org/10.1016/j.jallcom.2017.06.025>
- [54] Dhahri Khadija et al (2024) An in-depth insight at the percolation model and charge transport mechanism in $\text{La}_{0.7}\text{Ca}_{0.1}\text{Pb}_{0.2}\text{Mn}_{1-2x}\text{Al}_x\text{Sn}_x\text{O}_3$ manganite prepared by sol-gel route. *J Sol-Gel Sci Technol.* <https://doi.org/10.1007/s10971-024-06438-1>
- [55] Messai B, Makhloufi R, Keziz A, Benmakhlouf A, Nouiri M, Taha TAM (2025) Integrated study of morphology, structure, and dielectric behavior in PZT-SASF ceramics at the morphotropic phase boundary. *Ceram Int.* <https://doi.org/10.1016/j.ceramint.2025.01.496>
- [56] Wang S, Zhang X, Yao R, Fan L, Zhou H (2019) High-temperature dielectric relaxation behaviors in Mn_3O_4 polycrystals. *Materials* 12(24):4026–4026. <https://doi.org/10.3390/ma12244026>
- [57] Rout SK, Barhai PK, Sinha E, Hussain A, Kim W (2009) Anisotropic dielectric and electrical properties of hot-forged $\text{SrBi}_4\text{Ti}_4\text{O}_{15}$ ceramics. *Int J Appl Ceram Technol* 7:E114–E123. <https://doi.org/10.1111/j.1744-7402.2009.02453.x>
- [58] Djelil K, Keziz A, Rasheed M, Oueslati A (2025) SiO_2 's influence on the dielectric properties of natural fluorapatite-derived bio-compounds. *Ceram Int* 51(7):8658–8673. <https://doi.org/10.1016/j.ceramint.2024.12.296>
- [59] Miao G, Li N, Li P, Hao J, Li W, Du J, Fu P (2022) Analysis of complex impedance and electrical conductivity of $\text{YCr}_{0.5}\text{Mn}_{0.5}\text{O}_3\text{--CaCu}_3\text{Ti}_4\text{O}_{12}$ negative temperature coefficient ceramics. *Ceram Int* 48(17):24965–24978. <https://doi.org/10.1016/j.ceramint.2022.05.150>
- [60] Samantray NP, Choudhary P (2024) Studies of structural, dielectric and impedance spectroscopy of $\text{Bi}_4\text{Ti}_{2.8}\text{Sn}_{0.2}\text{O}_{12}$. *Ferroelectrics* 618(1):234–245. <https://doi.org/10.1080/00150193.2023.2271329>
- [61] Ghelloudj E, Keziz A (2025) Experimental failure analysis of AISI 4140 steel interconnecting shaft of the high-speed centrifugal compressor for regeneration gas. *Eng Fail Anal* 170:109283. <https://doi.org/10.1016/j.engfailanal.2025.109283>
- [62] Garoui I, Mallek M, Almutairi FN, Rekik W, Oueslati A (2024) Synthesis, structural characterization and complex impedance analysis of a novel organic-inorganic hybrid compound based on Mercury (II) chloride. *J Mol Struct.* <https://doi.org/10.1016/j.molstruc.2024.138881>

Publisher's Note Springer Nature remains neutral with regard to jurisdictional claims in published maps and institutional affiliations.

Springer Nature or its licensor (e.g. a society or other partner) holds exclusive rights to this article under a publishing agreement with the author(s) or other rightsholder(s); author self-archiving of the accepted manuscript version of this article is solely governed by the terms of such publishing agreement and applicable law.